sustainability

MDPI

Article

Assessing Ground Vibration Caused by Rock Blasting in Surface Mines Using Machine-Learning Approaches: A Comparison of CART, SVR and MARS

Gbétoglo Charles Komadja [1,2,3,*], Aditya Rana [2], Luc Adissin Glodji [3], Vitalis Anye [1], Gajendra Jadaun [2], Peter Azikiwe Onwualu [1] and Chhangte Sawmliana [2]

[1] Department of Materials Science and Engineering, African University of Science and Technology, Abuja 900001, Nigeria
[2] Rock Excavation Engineering Research Group, CSIR-Central Institute of Mining and Fuel Research, Barwa Road, Dhanbad 826001, India
[3] Department of Earth Sciences, University of Abomey-Calavi, Cotonou 01 BP 526, Benin
* Correspondence: gkomadja@aust.edu.ng

Abstract: Ground vibration induced by rock blasting is an unavoidable effect that may generate severe damages to structures and living communities. Peak particle velocity (PPV) is the key predictor for ground vibration. This study aims to develop a model to predict PPV in opencast mines. Two machine-learning techniques, including multivariate adaptive regression splines (MARS) and classification and regression tree (CART), which are easy to implement by field engineers, were investigated. The models were developed using a record of 1001 real blast-induced ground vibrations, with ten (10) corresponding blasting parameters from 34 opencast mines/quarries from India and Benin. The suitability of one technique over the other was tested by comparing the outcomes with the support vector regression (SVR) algorithm, multiple linear regression, and different empirical predictors using a Taylor diagram. The results showed that the MARS model outperformed other models in this study with lower error (RMSE = 0.227) and R^2 of 0.951, followed by SVR (R^2 = 0.87), CART (R^2 = 0.74) and empirical predictors. Based on the large-scale cases and input variables involved, the developed models should lead to better representative models of high generalization ability. The proposed MARS model can easily be implemented by field engineers for the prediction of blasting vibration with reasonable accuracy.

Keywords: mining; blasting; ground vibration; machine learning; multivariate adaptive regression splines

Citation: Komadja, G.C.; Rana, A.; Glodji, L.A.; Anye, V.; Jadaun, G.; Onwualu, P.A.; Sawmliana, C. Assessing Ground Vibration Caused by Rock Blasting in Surface Mines Using Machine-Learning Approaches: A Comparison of CART, SVR and MARS. *Sustainability* **2022**, *14*, 11060. https://doi.org/10.3390/su141711060

Academic Editor: Fernando António Leal Pacheco

Received: 16 June 2022
Accepted: 20 August 2022
Published: 5 September 2022

1. Introduction

The assessment and prediction of ground vibration generated by blasting is one important challenge in mine management. Blast-induced ground vibration (BIGV) is an unavoidable nuisance which, at a certain level, destroys the structural integrity of the surrounding structure in the mine area and affects far-field edifices. This results in complaints from the affected dwelling residents and mine closure with collateral consequences such as job losses and stalled socio-economic development. Sometimes, high-intensity BIGV can destroy groundwater tables, existing network conduits and the ecology of surrounding living communities (fauna and flora). Studies suggested that BIGV influences vegetation development and could contribute to deforestation in the near future [1]. The vibration induced by blasting usually leads to ground/slope instability, endangering the safety of workers during loading and subsequent drilling and blasting operations.

Although a lot of advancement has been witnessed over the decades in blasting technology, the undesirable effects of BIGV cannot be completely eradicated. However, it can be predicted and controlled to meet standard levels for damage minimization. Peak

particle velocity (PPV) induced by blasting is one of the best vibration indices that can effectively represent BIGV and potential damage to nearby structures [2]. The measurement of PPV using a seismograph is the only direct route, and is indubitably the most accurate measurement technique to assess the intensity of BIGV [3]. However, the method is expensive and time-consuming, and cannot predict PPV and prevent potential damages induced by blasting. Therefore, several scholars have developed indirect methods involving empirical formulas and machine-learning (ML) techniques to predict PPV [4]. The literature has revealed that several factors influence blasting PPV [5]. However, predictive empirical formulas involve only two parameters, namely maximum charge per delay and monitoring distance, and do not consider the complex interaction between PPV values and other blasting parameters, which undoubtedly leads to their low prediction capability [6]. The ML techniques have significantly improved the accuracy of PPV prediction in recent decades. ML techniques have the capability of solving complex engineering problems, and can handle more than a few effective input variables.

Studies by some researchers have applied ML techniques to predict PPV and optimize design parameters to reduce environmental, social, and economic impacts related to blasting vibration. For example, Shirani and Masoud [7] employed trial-and-error experimentation by combining gene-expression programming (GEP) and cuckoo optimization algorithm (COA) in an iron mine and achieved a significant reduction in PPV values (55.33%). Similarly, a combined method of principal component analysis (PCA) and support vector machine (SVM)-based PPV modeling was successfully used to optimize the blasting pattern in Hongtoushan Copper Mine in Vietnam [8]. Likewise, Bayat et al. [9] developed the artificial neural network (ANN) model optimized by the firefly algorithm (FA) to improve blast-design parameters. The results of their study yielded a 60% reduction in PPV which, in reality, could contribute to minimizing potential vibration impacts. Table 1 reports some studies employing ML techniques and empirical predictors in assessing PPV.

The review conducted by Dumakor-Dupey et al. [4] showed an excessive number of ML techniques applied in predicting PPV, with the common algorithms being artificial neural network (ANN), support vector machine (SVM), and the adaptive neuro-fuzzy inference system (ANFIS). The accuracy of the models depends upon the algorithm and the interaction between variables. Hybrid models have been recently introduced by combining two or more ML algorithms to enhance the accuracy of stand-alone ML techniques. However, these hybrid models result in complex mathematical expressions that are difficult to interpret and impracticable. These complex models are referred to as black-box techniques, in contrast to white-box techniques [10,11]. White-box techniques can provide interactive behavior between independent variables and the output. They are user-friendly and can be easily implemented on-site to optimize blast designs and control PPV. Therefore, this study aims to predict PPV based on two white-box ML techniques, such as classification and regression tree (CART) and multivariate adaptive regression splines (MARS), barely employed in previous studies (Table 1). In addition, different empirical methods, multiple linear regressions, and the adopted SVM algorithm, namely support vector regression (SVR), were also applied for comparison.

Although the literature shows that conventional white-box ML techniques can be easily implementable by field engineers to predict blast-induced outcomes, there are limited investigations applying CART and MARS to predict PPV. Monjezi et al. [12] reported that the generalization ability of predictive models increases with the number of input variables and datasets. Therefore, this study employed a record of 1001 sets of data from 34 different opencast mines to develop a single ML model. Each dataset involves ten blasting parameters of a wide range, including hole diameter (HDM), hole depth (HD), number of holes (NH), burden (B), spacing (S), stemming (T), charge per hole (CPH), total charge (TC), maximum charge per delay, (MCPD), and monitoring distance (D). These parameters are considered to be effective variables affecting blast-induced ground vibration (PPV) [5]. To the best of the authors' knowledge, there is no existing investigation involving many datasets and input variables from various geo-environments to develop regression

models for PPV prediction as employed in this study. Therefore, the investigation would obtain better results in representative models that could be implemented in different geo-environments for efficient prediction of PPV for safety and impact minimization. The overall study method is presented in Figure 1.

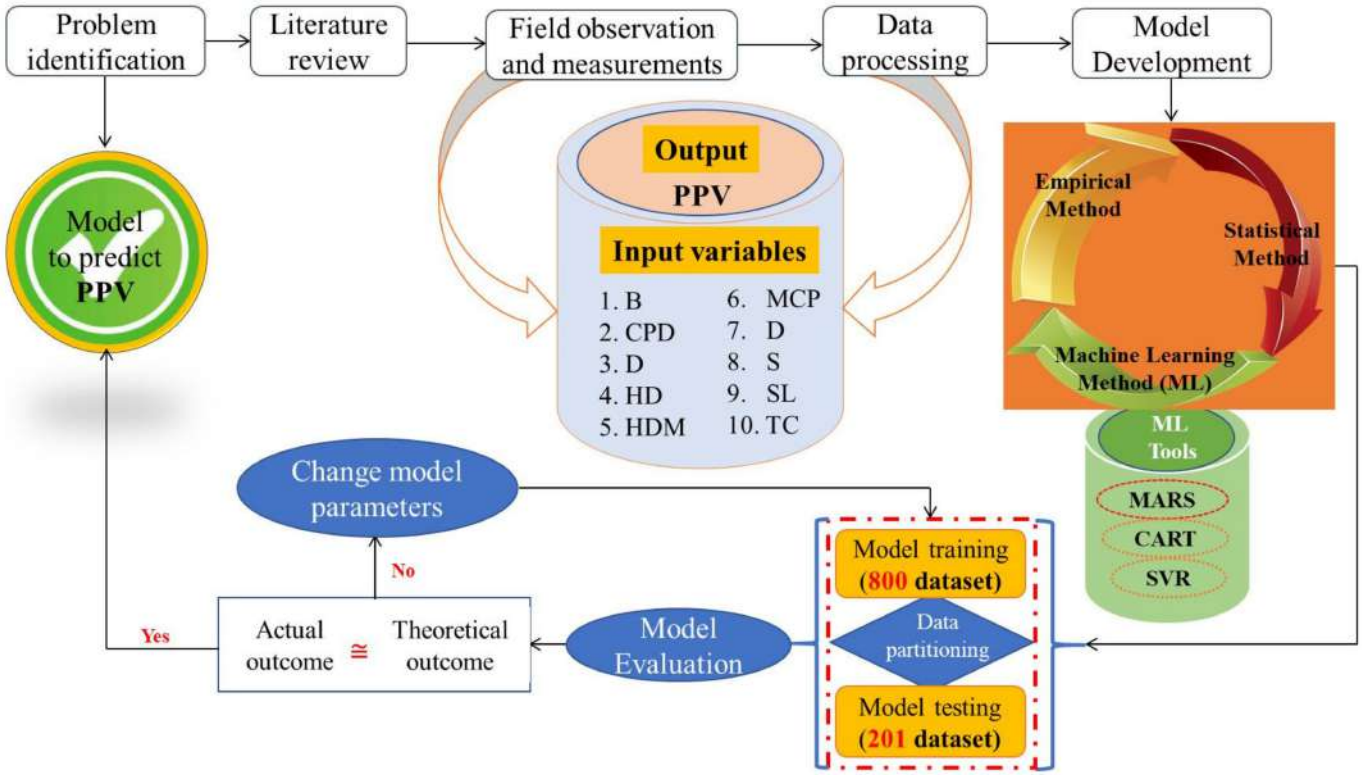

Figure 1. Flowchart of the overall study method.

This paper is structured as follows: after the introduction, the data source and a brief description of the different techniques employed to develop the models are presented in Sections 2–4, followed by the discussion and the results. The conclusion is presented in Section 5.

Table 1. Some studies of PPV prediction based on ML techniques.

Authors	Models	Input Parameters	No. of Datasets	Best Model	Performance Indices
Ke et al. [13]	SVR, GEP, ANN-SVR, Empirical predictor	HDM, BH, HD, B, S, Hc, PF, MCPD, D	297	ANN-SVR	R^2 = 0.887 RMSE = 1.232
Nguyen and Bui [14]	HGS–ANN, GOA–ANN FA–ANN, PSO–ANN	HD, MCPD, B, PF, D, SL, S NDS, DTS	252	HGS– ANN	R^2 = 0.922 RMSE = 1.761
Singh [15]	ANN	HDM, NH, HD, B, S, SL, Hdis, Rdis	200	ANN	R^2 = 0.83
Nguyen et al. [16]	MARS, ANN, PSO–ANN, MARS-PSO–ANN, Empirical predictor	MCPD, D, HD, B, S, SL, PF	193	MARS-PSO–ANN	R^2 = 0.902 RMSE = 1.569
Singh et al. [17]	ANFIS, MVRA	MCPD, D	192	ANFIS	R^2 = 0.98
Lawal et al. [18]	ANN, BK, GEP, MLR	S/B, BH/B, B/HDM, SL/B, SD/B, UCS, ρr, MCPD, D	191	ANN	R^2 = 0.948 RMSE = 0.0008

Table 1. *Cont.*

Authors	Models	Input Parameters	No. of Datasets	Best Model	Performance Indices
Singh and Verma [19]	ANFIS	B, S, D, IS, TC	187	ANFIS	R^2 = 0.77
Monjezi et al. [20]	ANN	HD, T, MCPD, D	182	ANN	R^2 = 0.949 (ANN)
Khandelwal and Singh [21]	ANN, MVRA	HD, S, D, E, P-wave, B, MCPD, BI, μ, VOD	174	ANN	R^2 = 0.98
Khandelwal [22]	SVM, MVRA, Empirical predictor	MCPD, D	174	SVM	R^2 = 0.96, MAE = 0.257
Khandelwal and Singh [23]	ANN	TC, D	170	ANN	R^2 = 0.998
Monjezi et al. [24]	MLPNN, RBFNN, GRNN	D, B/S, MCPD, NHPD, UCS, DPR	169	MLPNN	R^2 = 0.954, RMSE = 0.03
Yu et al. [25]	ELM, HHO–ELM, GOA–ELM,	D, HD, B/S, MCPD, PF	166	GOA–ELM	R^2 = 0.9105 RMSE = 2.855
Mohamed [26]	FS, ANN, MVRA	D, MCPD	162	FS	RMSE = 0.17 VAF = 87(%)
Bayat et al. [1]	GEP	B, S, T, D, MCPD	154	GEP	R^2 = 0.91 RMSE = 5.78
Khandelwal and Kumar [27]	ANN, Empirical predictor	MCPD, D	150	ANN	R^2 = 0.919, RMSE = 0.352
Singh et al. [28]	GA, MVRA, ANN, ANFIS, SVM	UCS, ρr, Hc, η, ABS, FRC	150	GA	MAPE = 0.198
Zhou et al. [29]	RF, ANN, XGBoost, AdaBoost, Bagging, Jaya-X-GBoost Empirical predictor	HDM, HD, CPH, S, B, CL, BI, E, D, μ, P-wave, VOD, ρe	150	Jaya-XGBoost	R^2 = 0.957 RMSE = 4.088
Mohamed [30]	ANN	P-wave, HDM, VOD, B, S, BH, HI, D, ρe, ρr, MCPD, E, TC, η, UCS,	149	ANN	R^2 = 0.94, MSE = 0.00920
Rana et al. [31]	CART, ANN, MVRA, Empirical predictor	TC, TS, MCPD, NH, HDM, D, HD, CPH	137	CART	R^2 = 0.95, RMSE = 1.56
Verma and Singh [32]	SVM, ANN, MVRA	HD, B, S, T, MCPD, TC, D	137	SVM	MAPE = 0.001
Verma and Singh [33]	GA, ANN, MVRA, Empirical predictor	HD, B, S, T, MCPD, TC	127	GA	R^2 = 0.99, MAPE = 0.088
Ghasemi et al. [34]	FS, MRA, Empirical predictor	B, S, T, NHPD	120	FS	R^2 = 0.945, RMSE = 2.73
Ghasemi et al. [35]	ANFIS-PSO, SVR	B, S, T, NH, MCPD, D	120	ANFIS-PSO	R^2 = 0.957, RMSE = 1.83
Bui et al. [36]	ANN, SVM, Tree-based ensembles, CSO–ANN Empirical predictor	MCPD, CPH, D, B, S, PF	118	CSO–ANN	R^2 = 0.99 RMSE = 0.246
Dehghani and Ataee-pour [37]	ANN, Empirical predictor, Dimensional analysis	S, B, DPR, NH, PF, D, CPD, MCPD, PLI	116	ANN	R^2 = 0.945, RMSE = 0.0245

Table 1. *Cont.*

Authors	Models	Input Parameters	No. of Datasets	Best Model	Performance Indices
Zhongya [38]	BPNN, MVRA, ELM-FA MIV	D, MCPD, B/S, NHPD, UCS, DPR	108	ELM-FA MIV	R^2 = 0.96, RMSE =0.21
Armaghani et al. [39]	MPMR, LSSVM, GPR PSO–ELM, AGPSO–ELM	B/S, MCPD, D, T, PF, HD	102	AGPSO–ELM	R^2 = 0.90 RMSE = 0.08
Faradonbeh et al. [40]	GEP, NLMR	T, B/S, PF, D, HD, MCPD	102	GEP	R^2 = 0.874
Mokfi et al. [41]	GMDH, GEP, NLMR	MCPD, PF, T, B/S, D, HD	102	GMDH	R^2 = 0.874, RMSE = 0.963
Ismail et al. [42]	GEP, ANFIS, SCA-ANN Empirical predictor	D, MCPD, ρr, SRH	100	SCA-ANN	R^2 = 0.999 RMSE = 0.0094
Hajihassani et al. [43]	ICA-ANN, ANN, MLR	B/S, T, MCPD, P-wave, E, D	95	ICA-ANN	R^2 = 0.97
Chen et al. [44]	FA–SVR, PSO–SVR, GA–SVR, FA–ANN, PSO–ANN, GA–ANN, MFA–SVR	B/S, T, MCPD, D, E, P-wave	95	MFA–SVR	R^2 = 0.984 RMSE = 0.614
Peng et al. [45]	ANN, ANN-PSO, ANN-GA, ANN	MCPD, D, PF, SD, RQD, B, S	93	ANN-PSO	R = 0.945 RMSE = 0.680
Hasanipanah et al. [46]	CART, MLR, Empirical predictor	MCPD, D	86	CART	R^2 = 0.95, RMSE = 0.17
Hudaverdi and Akyildiz [47]	ANN, MLR Empirical predictor	MCPD, D, B, S	86	ANN	RMSE = 5.28
Zhu et al. [48]	ANN, ANFIS, RANFIS CRANFIS, CRANFIS-PSO, Empirical predictor	B, S, T, PF, MCPD, D	84	CRANFIS-PSO	R^2 = 0.997 RMSE = 0.076
Shahnazar et al. [49]	PSO-ANFIS, ANFIS	D, MCPD	81	ANFIS-PSO	R^2 = 0.984, RMSE = 0.4835
Hasanipanah et al. [50]	SVM, Empirical predictor	MCPD, D	80	SVM	R^2 = 0.96, RMSE = 0.34
Abbaszadeh Shahri et al. [51]	GFFN-FA, GFFN-ICA, GFFN	B, S, TC, D, MCPD	78	GFFN-FMA	R^2 = 0.97 RMSE = 0.187
Saadat et al. [52]	ANN, Empirical predictor	MCPD, D, SL, HD	69	ANN	R^2 = 0.95, RMSE = 8.79
Álvarez-Vigil et al. [53]	ANN, MLR	RMR, BCPRA, D, HDM, S, HD, B, MCPD, VOD, TC, NH	60	ANN	R^2 = 0.96, RMSE = 0.65
Lawal et al. [3]	ANN, GEP, MFO-ANN, MLR, Empirical predictor	HD, CPD, NH, TC, D, RMR	56	MFO-ANN	R^2 = 0.957 MSE = 0.0008
Amini et al. [54]	ANN	D, ρe Ve, B, S, TC	51	ANN	R^2 = 0.96
[55]	CART, MR, Empirical predictor	MCPD, D	51	CART	R^2 = 0.92, RMSE = 0.97
Iphar et al. [56]	ANFIS, MLR	MCPD, D	44	ANFIS	R^2 = 0.98, RMSE = 0.80

Table 1. *Cont.*

Authors	Models	Input Parameters	No. of Datasets	Best Model	Performance Indices
Armaghani et al. [57]	BP-ANN, PSO–ANN	HDM, HD, MCPD, S, B, SL, PF, ρr, SD, NR	44	PSO–ANN	R^2 = 0.93
Lapčević et al. [58]	ANN	CPH, DT, MCPD, TC, D	42	ANN	R^2 = 0.95
Mohamadnejad et al. [59]	SVM, GRNN, Empirical predictor	MCPD, D	37	SVM	R^2 = 0.89, RMSE = 1.62
Monjezi et al. [60]	GEP, MLR, NLMR	D, MCPD	35	GEP	R^2 = 0.918, RMSE = 2.321
Li et al. [61]	SVM, Empirical predictor	MCPD, D	32	SVM	R^2 = 0.945
Ravilic et al. [62]	MCPD, D, TC	ANN, Empirical predictor	32	ANN	R^2 = 0.9 RMSE = 0.018
Monjezi et al. [12]	ANN, Empirical predictor	TC, MCPD, D	20	ANN	R^2 = 0.924, RMSE = 0.071
Ragam and Nimaje [63]	GRNN, Empirical predictor	D, MCPD	14	GRNN	R^2 = 0.999, RMSE = 0.0001

2. Materials and Methods

2.1. Materials

The dataset used for this research work was gathered from 34 opencast mines. Table 2 presents the different mines/quarries along with the excavation materials. The blasting operations and the output, such as the induced vibration, flyrock and air overpressure from the different sites, are under monitoring by the rock excavation engineering division of the Central Institute of Mine and Fuel Research India (CSIR-CIMFR). In addition, the largest granite aggregate quarry, namely OKOUTA CARRIERE SA, located in Setto, Benin, was considered in this study. Thousands of blasting data were compiled and subjected to curation. After filtering, 1001 complete measured peak particle velocities with ten corresponding blast-design parameters, i.e., hole diameter (HDM), hole depth (HD), number of holes (NH), burden (B), spacing (S), stemming (SL), charge per hole (CPH), total charge (TC), maximum charge per delay, (MCPD), and monitoring distance (D), were considered to establish the models. Table 3 presents the descriptive statistics of the input and output variables. The correlation between input variables and target PPV can be seen from the Pearson correlation matrix presented in Figure 2. It can be noticed that there is no collinearity between the predictor variables and the output PPV that can significantly influence model efficiency. To further evaluate how sensitive the output response PPV is to the independent variables, sensitivity analysis was performed using cosine amplitude technique [64]. The cosine amplitude can be obtained using the following expression (Equation (1)). The value of r_{ij} closer to unity indicates significant influence of the input variable on the output PPV. Figure 3 shows the relative strength of all input variables to PPV. The value of r_{ij} ranges between 0.605 to 0.902, suggesting that all the input variable influences the response PPV. Because each variable has a relative influence (r_{ij} > 0.6) on the output variable PPV, all 10 predictor variables were used to establish the models.

$$r_{ij} = \frac{\sum_{k=1}^{n} (Y_{ik} * Y_{ok})}{\sqrt{\sum_{k=1}^{n} Y_{ik}^2 \sum_{k=1}^{n} Y_{ok}^2}} \quad (1)$$

where Y_i and Y_o are the inputs and output, respectively.

Table 2. List of the investigated mines/quarries for data-gathering.

No.	Mines	Company
1	Chandan Coal Mine, Jharia	Bharat Cooking Coal Limited
2	Patherdih Coal Mine, Jharia	Bharat Cooking Coal Limited
3	Bera Coal Mine, Bastacola	Bharat Cooking Coal Limited
4	Golakdih Coal Mine, Bastacola	Bharat Cooking Coal Limited
5	Jogidih Coal Mine, Govindpur	Bharat Cooking Coal Limited
6	Dahibari Coal Mine, Chanch Victoria Area	Bharat Cooking Coal Limited
7	Gopalichuk Coal Mine, Pootkee Balihari Area	Bharat Cooking Coal Limited
8	Bagdigi Coal Mine, Lodna	Bharat Cooking Coal Limited
9	Tetulmari Coal Mine, Sijua Area	Bharat Cooking Coal Limited
10	Kujama Coal Mine, Bastacola	Bharat Cooking Coal Limited
11	Bhanora Coal Mine, Sripur area	Eastern Coalfields Limited
12	Magadh Coal Mine, Magadh Amrapali Area	Central Coalfields Limited
13	Pakri Barwadih Coal Mine, Barakagaon	National Thermal Power Corporation
14	Tasra Coal Mine, Jharia	Steel Authority of India Limited
15	Bermo Coal Mine, Bokaro	Damodar Valley Corporation
16	Jamuna Coal Mine, Jamuna and Kotma Area	South Eastern Coalfields Limited
17	Ramagundam-III Area Coal Mine, Peddapalli	Singareni Collieries Company Limited
18	Aditya Cement Limestone Mine, Shambhupura	M/S Ultratech Cement
19	Adhunik Cement Limestone Mine, Meghalaya	Adhunik Cement Limestone Mine
20	Manal Limestone Mine, Rajban	Cement Corporation of India Limited
21	Daroli Limestone Mine, Udaipur	Daroli Limestone Mines
22	SK2 Block Vikram Limestone Mine, Khor	Vikram Cement works
23	Karunda Limestone Mine, Chittorgarh	J K Cement
24	Malikhera Limestone Mine, Chittorgarh	J K Cement
25	Murlia Block Limestone Mine, Chandrapur	Murli Industries Limited
26	Jhamarkotra Rock Phosphate Mine, Udaipur	Rajasthan State Mines and Minerals Limited
27	Sanchali Calcite Mine, Udaipur	M/s Wollmine India Pvt. Limited
28	Guali Iron Ore Mine, Topadihi	M/s R. Sao
29	Narayanposhi Iron and Manganese Ore Mine Koria, Sundergarh	M/s Aryan Mining and Trending Corp. Limited
30	Balda Block Iron Ore Mine, Keonjhar	M/s Serajuddin and Company, Orissa
31	Banduhurang Opencast Uranium Mines	Uranium Corporation of India Limited
32	Obra Stone Mine (Dolomite quarry)	M/s B. Agarwal Stone Products Limited, Sonebhadra
33	Pachami Hatgacha Stone Mining, Birbhum	West Bengal Mineral Development and Trading Corporation Limited
34	Granite aggregate quarry, Setto, Benin republic	OKOUTA CARRIERES SA

Table 3. Descriptive statistics of the input and output variables.

Parameters	Unit	Symbol	Category	Min	Max	Mean	Median	Sd. Dev
Hole diameter	mm	HDM	Input	32	269	126.5	115	32.04
Hole depth	m	HD	Input	0.7	13.5	6.59	6.2	2.28
Number of holes	-	NH	Input	1	199	31.52	21	33.06
Burden	m	B	Input	0.6	9	3.13	3	1.05
Spacing	m	S	Input	0.6	10	4.04	3.5	1.52
stemming length	m	SL	Input	0.5	7	3.04	3	0.94
Charge per hole	kg	CPH	Input	0.17	400.75	39.2	32.14	36.49
Total charge	kg	TC	Input	5.56	41294	1390.86	544.46	2767.81
Maximum charge per delay	kg	MCPD	Input	2.19	2545.5	85.92	45.5	169.98
Monitoring distance	m	D	Input	25	1500	321.36	293	185.45
Peak particle velocity	mm/s	PPV	Output	0.22	43.59	3.37	2.44	3.12

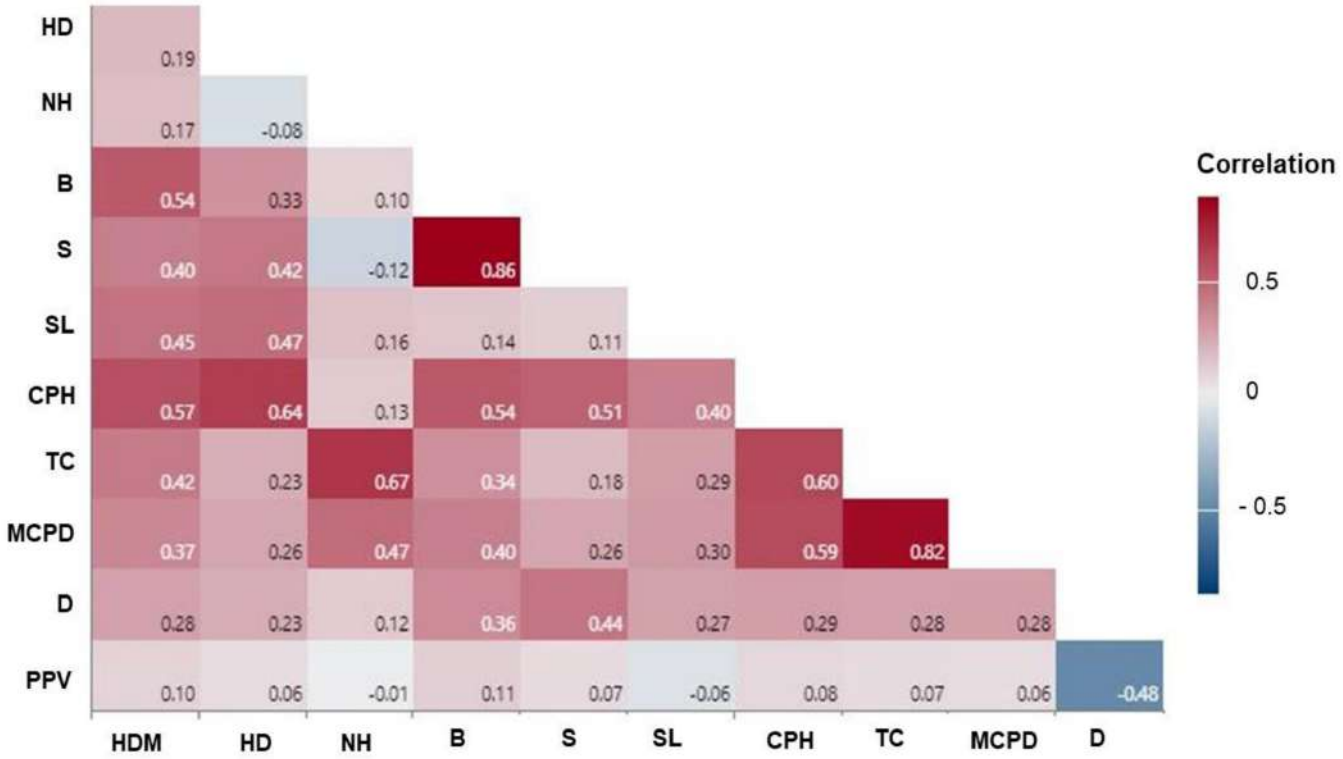

Figure 2. Correlation matrix of PPV dataset.

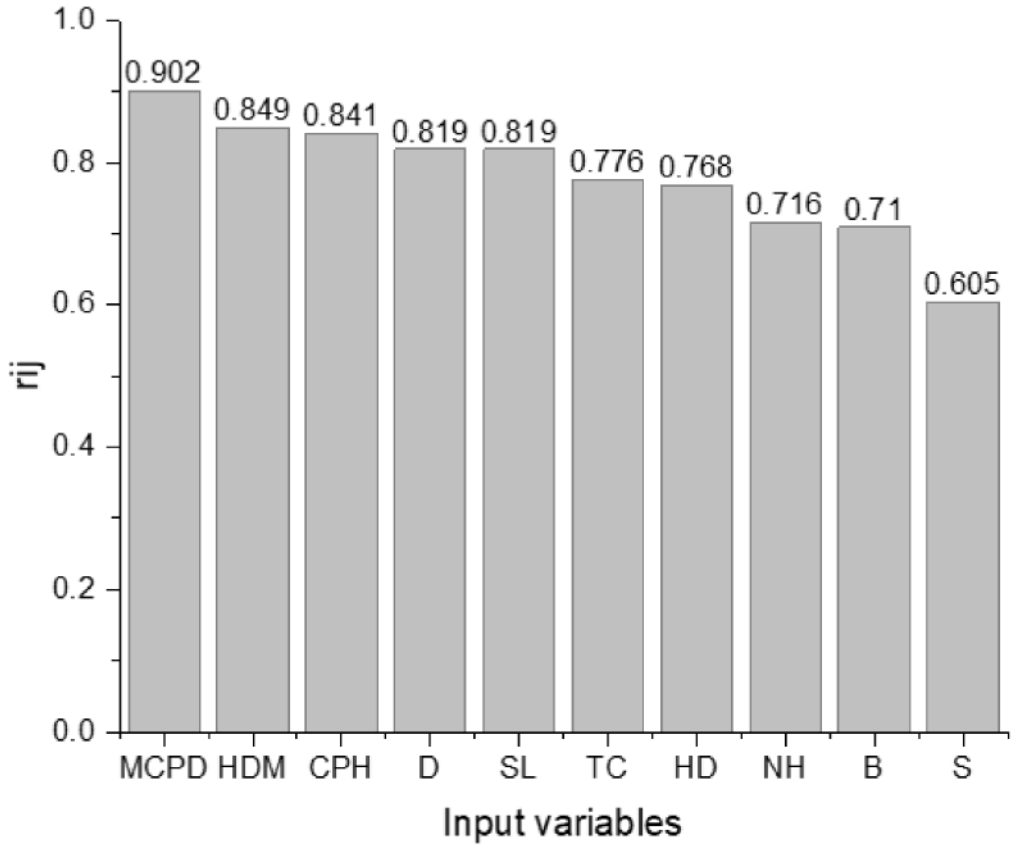

Figure 3. Sensitivity analysis of the input variables on PPV.

2.2. Methods

This section presents a brief description of the proposed models applied in the present study. As mentioned earlier, 1001 data points were randomly split into two sets, namely training and testing. The training set comprises 800 datasets, i.e., 80% of all the data points, and was employed to calibrate the models. The remaining 20% (201 datasets) was used to test the models. Two white-box machine-learning techniques, namely CART and MARS, were developed. In addition, the traditional SVR algorithm, as well as MLR and different empirical predictors, were used for comparison.

2.2.1. Empirical Methods

Several empirical equations have been developed to predict PPV. Scaled distance-based-empirical predictors involving maximum charge per delay and distance between blasting and measuring point have been suggested for the prediction of blast-induced PPV. The performance of five commonly used empirical methods, as presented in Table 4, was evaluated on the dataset used in this research.

Table 4. Some PPV predictive methods based on empirical equations.

Name	Equations
USBM	$PPV = K\left(\boldsymbol{D}/\sqrt{\boldsymbol{MCPD}}\right)^{-B}$
Langefors–Kihlstrom (L–K)	$PPV = K\left(\sqrt{\boldsymbol{MCPD}/D^{2/3}}\right)^{B}$
Ambraseys–Hendron (A–H)	$PPV = K\left(\frac{\sqrt[3]{\boldsymbol{MCPD}}}{\boldsymbol{D}}\right)^{B}$
IS	$PPV = K\left(\boldsymbol{MCPD}/D^{2/3}\right)^{B}$
CMRI	$PPV = n + K\left(D/\sqrt{\boldsymbol{MCPD}}\right)^{-1}$

The site coefficients '*K*', '*A*', '*B*', and '*n*' as presented in the equations are site-specific and can be obtained using multiple regression.

2.2.2. Multiple Linear Regression (MLR)

MLR is a statistical method used to model the relationship between two or more predictors (input variables) and one outcome variable by fitting a linear equation. Every input variable x (independent variable) is associated with a value of the response y (dependent variable). Here the blast-design parameters in Table 3 represent the predictor variables and the output response PPV. MLR assumes that the relationship between predictor variables and the output response is linear. MLR can be mathematically expressed as in Equation (2).

$$\boldsymbol{y} = \boldsymbol{\beta_0} + \boldsymbol{\beta_1 x_1} + \boldsymbol{\beta_2 x_2} + \ldots. + \boldsymbol{\beta_n x_n} + \boldsymbol{e} \quad (2)$$

where $\boldsymbol{y}$ stands for the output response, $\boldsymbol{x_i}$ $(\boldsymbol{i} = \boldsymbol{1}, \boldsymbol{2}, \ldots\ldots, \boldsymbol{n})$ denotes the input variables, $\boldsymbol{\beta_i}$ $(\boldsymbol{i} = \boldsymbol{0}, \boldsymbol{1}, \boldsymbol{2}, \ldots\ldots, \boldsymbol{n})$ are the regression coefficients, and $\boldsymbol{e}$ the prediction error.

2.2.3. Classification and Regression Tree (CART)

The classification and regression tree, known as CART, is one of the decision-tree algorithms that has been in use for about 40 years [65] and remains a popular machine-learning tool. CART operates using recursive partitioning of the data to break it up into smaller parts. It is a non-parametric method, with the capability of handling high-dimensional data without any prior normalisation. A CART model output is represented as an inverted tree, with a main root node and internal nodes that end up with a terminal node (Figure 4).

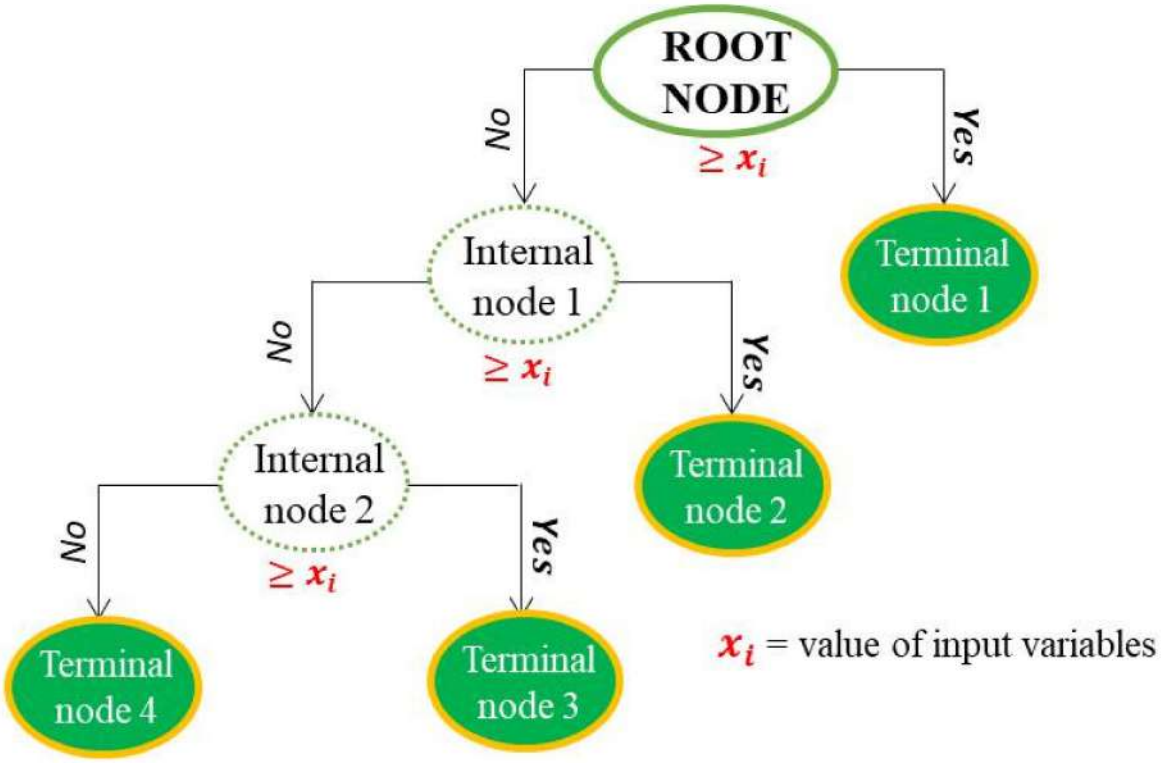

Figure 4. Example of a simple decision tree.

The root node depicts the most influential input variable on the output. From the root node, CART evaluates all possible splits of all predictor variables, classifies them, and selects the "greatest" single split overall. The best split of the variable designated is better than the best split of any other predictor with the minimum sum of squares and placed at an internal node. The internal node has relatively more cases and is further partitioned based on the same sum-of-squares criterion until a terminal node is reached relatively homogenously. In binary partitioning, the best predictor at each internal node splits the data into two subsets using yes/no or if/then rules. The terminal node represents a prediction value of the response based on the set decision rules. The number of internal nodes depends on the complex interaction between the input variables and the output. Assuming a partition into R regions, R_1, R_2..., R_m and the output as a constant Cm in each region, the adaptive basis function framework of the recursive partitioning can be represented as in Equation (3) [66].

$$f(x) = \sum_{m=1}^{M} C_m I(x \in R_m) \quad (3)$$

where R_m is the mth region and C_m is the mean response in a given region (scalar for regression, class probabilities for multi-class classification).

One of the challenges of CART, as with any other decision-tree algorithm, is the difficulty of obtaining the optimum tree that represents the data. A small tree is easy to interpret, but may lack information on the important structure of the data, whereas an overgrowing tree might overfit the data and be difficult to understand. There are several processes to reach the optimum tree for a given dataset, and the common approach is to grow the full tree and subject it to the pruning process [67].

2.2.4. Support Vector Regression (SVR)

Support vector regression is a regression algorithm derived from support vector machine (SVM). Initially, the algorithm was developed by Cortes and Vladimir [68] for

classification purposes and later extended to solve regression problems for continuous values and designated as SVR. Unlike a simple linear regression, where the algorithm works to minimize the error rate, SVR tries to fit the error within a certain margin of tolerance (epsilon). The threshold limit is defined by two boundary lines away from the reference data which fit the maximum data points, known as the hyperplane. The epsilon is a hyperparameter used to tune the model. Figure 5 illustrates a one-dimensional SVR technique where the data points represent the predicted values along with the best fit (hyperplane). The data points, which determine the direction of the boundaries, are termed support vectors. The support vectors participate in finding a match between the data point and the hypothesis function that defines the best fit of the data (hyperplane). Assuming the hyperplane is a straight line toward the $\boldsymbol{y}$ axis, the hypothesis function of the hyperplane can be expressed as presented in Figure 5, as well as the expression of the two boundary limits. SVR tries to find the maximum margin that best fits the hyperplane by constraining the errors to the acceptable threshold limit defined as the maximum error ($\boldsymbol{\epsilon}$, epsilon). On the other hand, the algorithm tends to satisfy the condition $-\boldsymbol{\epsilon}<\boldsymbol{y}-(\boldsymbol{wx}+\boldsymbol{b})<+\boldsymbol{\epsilon}$ stating the fact that $y = Wx + b = 0$. The epsilon parameter is used to optimize the model by constraining the error as $|\boldsymbol{y_i}-\boldsymbol{w_i x_i}| \leq \boldsymbol{\epsilon}$. The slope w (learned weight vector) helps to optimize the margin $|\epsilon|$ by reducing the distance ζ between the margin limits and predicted values outside the bounds. The objective function is to maximize the margin (minimizing ζ, $\zeta \geq 0$) within the acceptable error tolerance ($|y_i - w_i x_i| \leq \epsilon + |\zeta_i|$) to obtain the optimal hyperplane, and is expressed as in Equation (4).

$$\boldsymbol{min}\ \frac{1}{2}||\boldsymbol{w}||^2 + \boldsymbol{C}\sum_{\boldsymbol{i}=1}^{\boldsymbol{n}} |\boldsymbol{\zeta_i}| \tag{4}$$

where $y_i, \in \mathbb{R}$ is the response variable, w_i is the weight vector, and $x_i, \in \mathbb{R}$ is the training input variable. $\boldsymbol{C}$ is another tuning parameter that controls the error margin defined by ϵ and the weight vector $|\boldsymbol{w}|$.

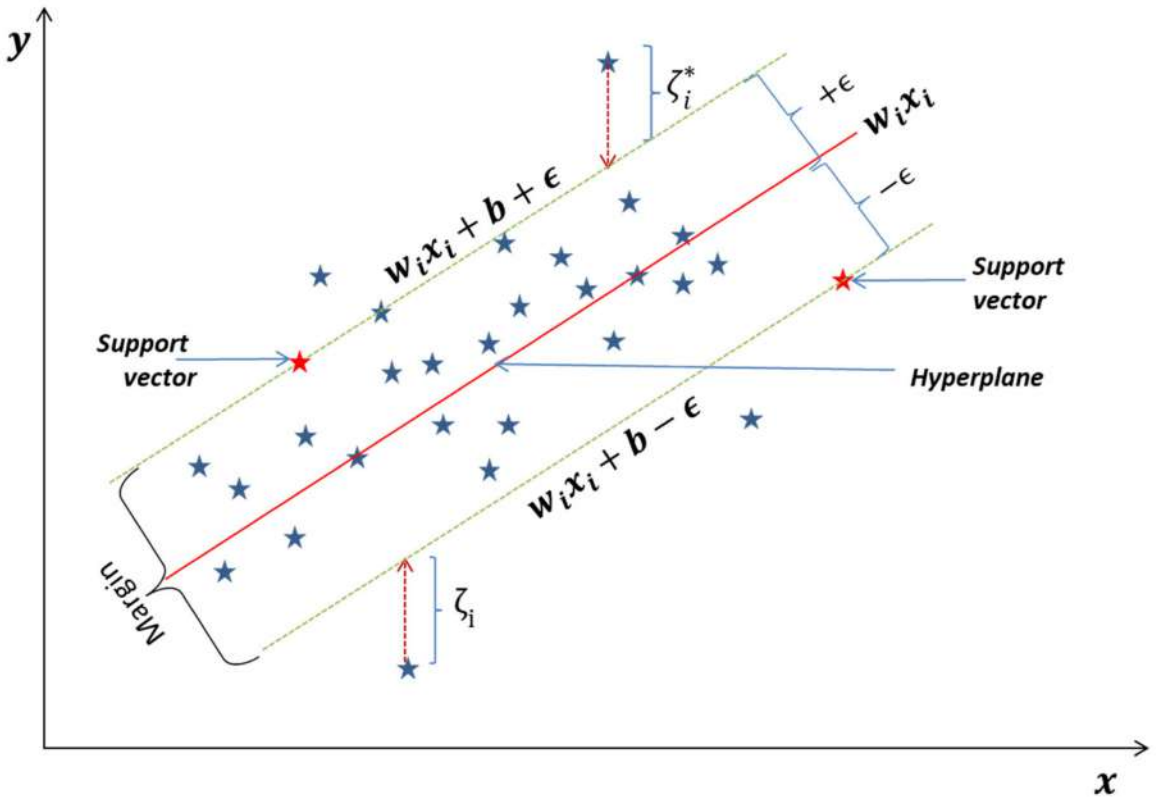

Figure 5. Schematic illustration of one-dimensional SVR.

For a non-linear regression, as is the case in the present study, a kernel function is used to transform the data to higher-dimensional feature space and perform linear separation. Gaussian Radial Basis Function (RBF) is widely used for non-linearity relationships between predictors and response variables, and was adopted in this study. The equation of RBF is as follows (Equation (5)).

$$k(x,\ x_i) = exp\left(-\frac{||\boldsymbol{x} - \boldsymbol{x_i}||^2}{2\sigma^2}\right) \quad (5)$$

where σ is the kernel RBF parameter that must be tuned during the calibration of the model.

2.2.5. Multivariate Adaptive Regression Splines (MARS)

MARS is a non-parametric ensemble machine-learning regression technique method designed for multivariate non-linear regression problems. The algorithm can split the data into several intervals (splines) depending on the variable's pattern. Each spline represents a linear function that best characterizes the data. A MARS model can be viewed as an ensemble of linear functions referred to as splines or basis functions (BFs) as illustrated in Figure 6. The end of a spline and the beginning of another is denoted as a knot. Two general steps describe the functionality of a MARS model: a forward procedure followed by a backward procedure. In the forward stage, the algorithm splits the data into an excessive number of splines, which may lead to an overfit model. The backward step is a pruning procedure where all the splines that poorly contribute to the overall model performance are automatically deleted [69]. The generalized MARS model with appropriate knots can be expressed using the combination of the weighted BFs of all the linear splines [70] as in Equation (6).

$$f(x) = \beta_0 + \sum_{n=1}^{n=N} \beta_n BF(x) \quad (6)$$

where N is the total number of splines BFs during the forward stage, β_0, and β_n, are the intercept and the weighting coefficients of the nth splines (BF), respectively, and are estimated using the least-squares method.

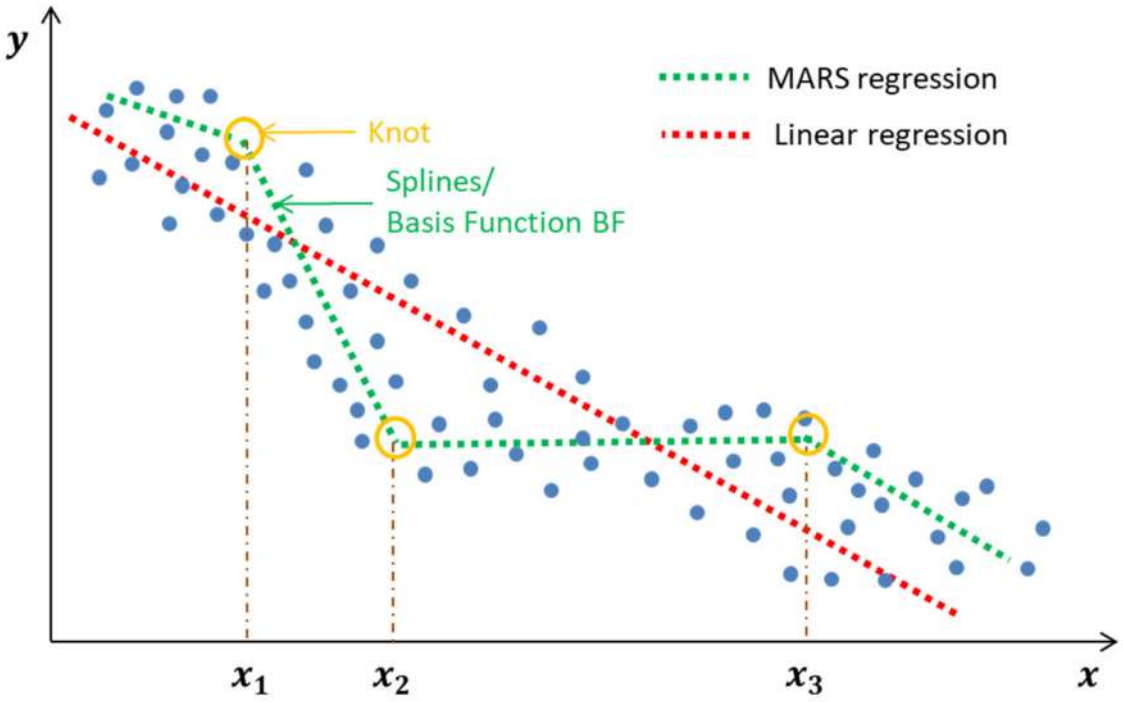

Figure 6. Relationship between a set of predictors x_i and an output variable y.

The performance of the model in the pruning stage is evaluated using generalized cross-validation (*GCV*) on the training dataset. *GCV* error includes both residual error and model complexity [71]. A MARS model with the lowest *GCV* error is considered the optimal model. The *GCV* can be mathematically expressed as in Equation (7) [66].

$$GCV = \frac{1}{N}\sum_{n=1}^{n=N}(Y_n - f(x_n))^2 / \left(1 - \frac{C}{N}\right)^2 \quad (7)$$

with $C = r + p * d$

where N is the number of observations, $f(x_n)$ is the estimated output variable by the nth piecewise linear function (*BF*s) (n = 1, 2,..., N), Y_n is the nth measured output variables, C is an effective number of parameters, where r denotes the number of independent *BF*s, d the number of knots during the forward stage, and p the penalty for adding a *BF*.

3. Results

The present paper adopts two statistical indices, namely co-efficient of determination ($R2$) (Equation (8)) and root means square error (RMSE) (Equation (9)), to assess the optimum model and evaluate the relationship between the measured and predicted PPV value based on the proposed models.

$$R2 = 1 - \frac{\sum_{i=1}^{n}(y_i - \hat{y}_i)^2}{\sum_{i=1}^{n}(y_i - \overline{y}_{i.})^2} \quad (8)$$

$$RMSE = \sqrt{\frac{1}{n}\sum_{i=1}^{n}(\hat{y}_i - y_i)^2} \quad (9)$$

y_i represents the measured PPV, $\hat{y}_i$ is the predicted PPV from the model, $\overline{y}_{i.}$ represents the average value of the measured PPV, and n the number of samples in the training or testing stages.

All the models were developed using Python (Anaconda3) codes through a Spyder environment. Overall, 800 training datasets were used to fit the models, whereas 201 independent datasets were employed for model testing.

3.1. MLR

The multiple linear regression equation based on the training dataset is presented in Equation (10).

$$\begin{aligned} PPV = {} & 1.9830 + 0.0171 \times HDM + 0.2007 \times HD - 0.0053 \times NH + 0.0350 \times B + 0.5605 \times S - 0.101 \times SL \\ & - 0.01635 \times CPH + 0.0003 \times TC - 0.000019 \times MCPD - 0.011698 \times D \end{aligned} \quad (10)$$

Table 5 reports the analysis of variance (ANOVA) of the fit model. The trained model (Equation (10)) was assessed using unseen data (test data). The performance between the measured and predicted PPV values is presented in Figure 7. As it can be seen, the MLR model yielded an R^2 of 0.384 and 0.4 for training and testing, respectively. This shows that MLR poorly explains the relationship between PPV and the predictor variables and confirms the non-linear interaction between variables.

Table 5. MLR model output.

Parameters	Coefficients	Standard Error	t Stat	*p*-Value
Intercept	1.9830	0.5470	3.6254	0.0003
HDM	0.0171	0.0044	3.8961	0.0001
HD	0.2007	0.0622	3.2266	0.0013
NH	−0.0053	0.0042	−1.2416	0.2148

Table 5. *Cont.*

Parameters	Coefficients	Standard Error	t Stat	*p*-Value
B	0.0350	0.2057	0.1704	0.8648
S	0.5605	0.1422	3.9411	0.0001
SL	−0.1010	0.1309	−0.7714	0.4407
CPH	−0.0163	0.0048	−3.4138	0.0007
TC	0.0003	0.0001	4.2827	0.0000
MCPD	−0.000019	0.0009	−0.0205	0.9837
D	0.011698	0.0006	−20.6706	0.0000

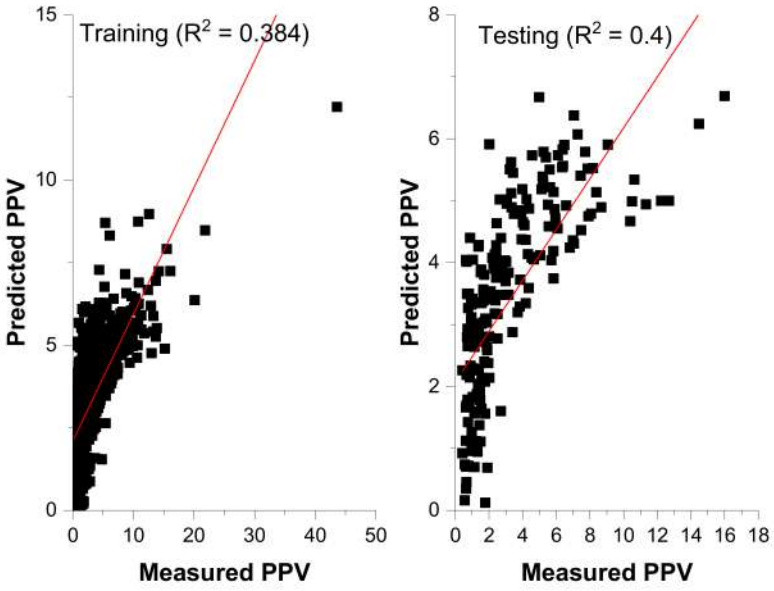

Figure 7. Measured versus Predicted PPV by MLR.

3.2. Empirical Methods

Scaled law and several modified empirical equations based on charge quantity and distance between blasting and measuring point have been suggested for measuring blast-induced PPV. As mentioned earlier, the empirical methods involve site coefficients and 80% of all the datasets (801 datasets) termed training data was employed to determine the site constants. The remaining 20% (201 datasets) was considered to be testing for model performance evaluation. Using regression analysis, the site coefficients were obtained and reported in Table 6. The obtained coefficients were employed to predict PPV using an independent dataset (testing dataset). Figure 8a–e present the fitting curves between the measured and the predicted PPV for different empirical methods employed. The performance indices (Table 6) indicate that the Ambraseys–Hendron equation yielded the highest R^2 on the testing dataset, followed by the USBM and CMRI predictor, respectively.

Table 6. Computed site constants and performance indices from empirical predictors.

Name/References	Constant Coefficients			Performance Indices			
				Training		Testing	
	K	B	n	RMSE	R^2	RMSE	R^2
USBM	66.676	0.902	-	2.369	0.467	0.918	0.630
L-K	1.567	0.220	-	2.370	0.062	1.405	0.096
A-H	211.910	1.034	-	2.328	0.513	0.855	0.673
IS	2.313	0.346	-	3.213	0.150	1.324	0.223
CMRI	85.482	-	0.478	2.318	0.471	0.890	0.622

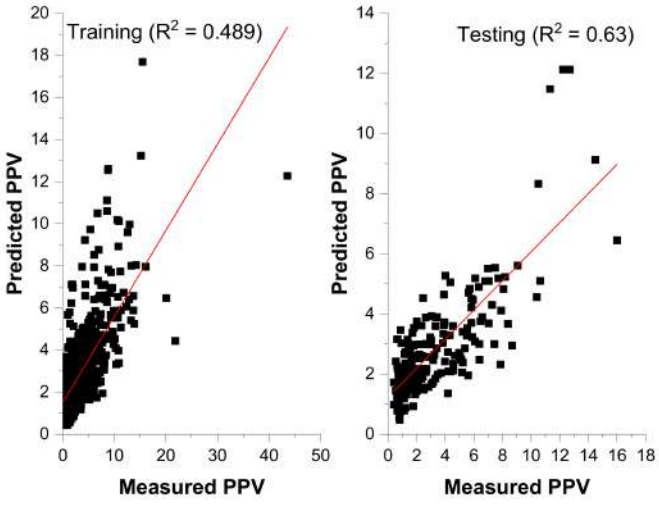

(**a**)

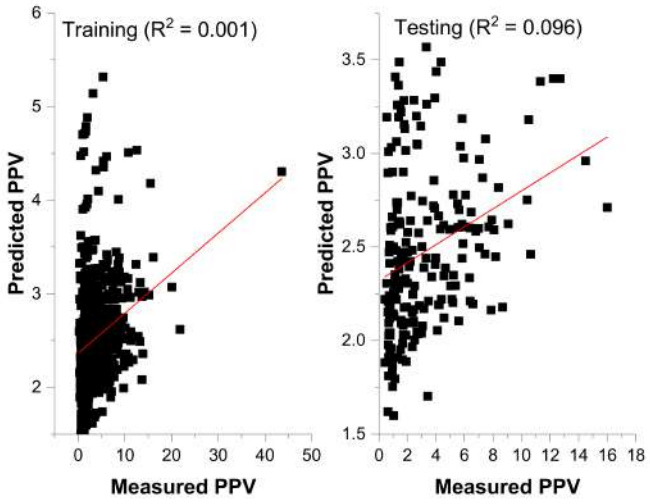

(**b**)

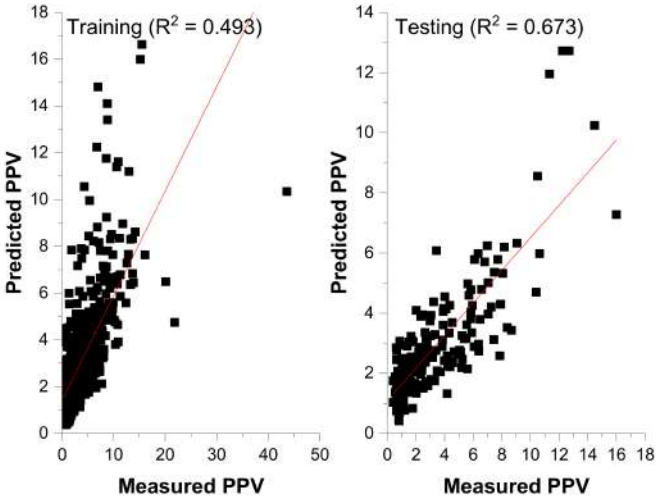

(**c**)

Figure 8. *Cont*.

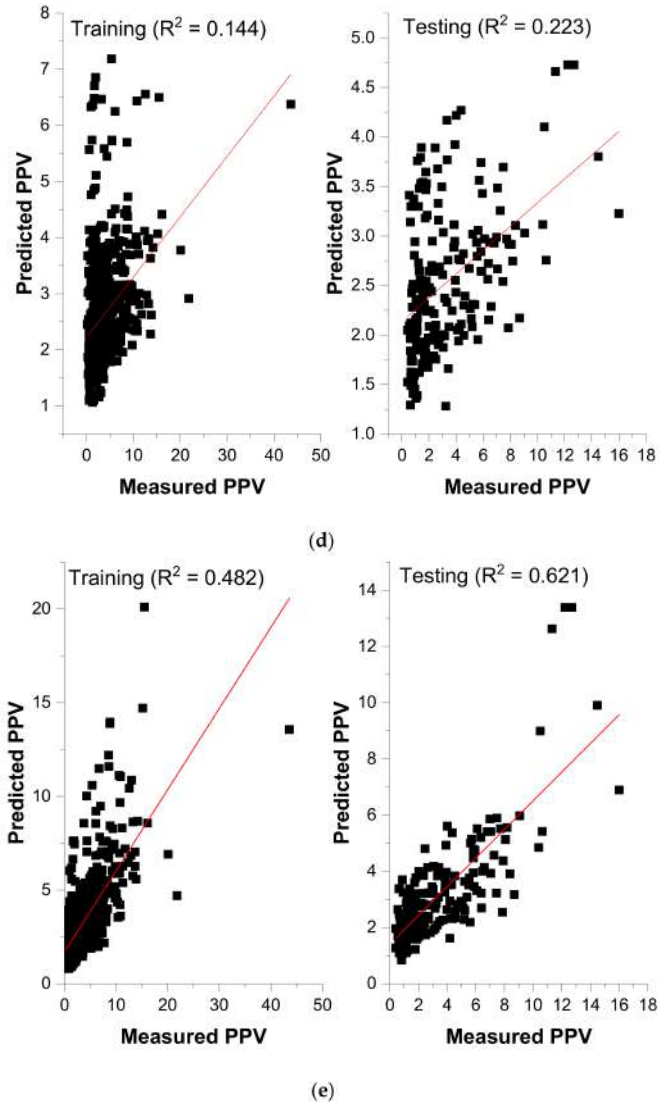

Figure 8. (**a**) Measured versus Predicted PPV (USBM Method). (**b**) Measured versus Predicted (L–K method). (**c**) Measured versus Predicted (A–H). (**d**) Measured versus Predicted (IS method). (**e**) Measured versus Predicted (CMRI method).

3.3. CART Model for the Prediction of PPV

The CART model was built using the Python Scikit-learn package through the Spyder (Anaconda3) environment. Scikit-learn uses an optimized version of the CART algorithm. Initially, the default parameters were employed to grow the full tree. Cost–complexity pruning analysis is widely employed to prune regression trees. The parameters cost–complexity and pruning-alpha (ccp_alpha) were employed to prune the obtained tree. The default value of ccp_alpha is zero, corresponding to the complex initial tree to be pruned. The complexity of the tree decreases with the increase of ccp_alpha $\in$ R (R $\geq$ 0). The optimal tree is the subtree with the largest cost–complexity and lowest error on unseen data (test data). Figure 9 presents the error (RMSE) trend on both the training and testing datasets for varying values of ccp_alpha. As can be expected, the error increases as the ccp_alpha values increase. A relatively steady level can be seen from 0.009 to 0.012 on the training error curve (Figure 9) with the lowest RMSE of 0.524 at ccp_alpha 0.01. A rational error (RMSE) of 1.139 and R^2 of 0.744 was obtained on the testing dataset (Figure 9 and Table 7). Therefore, the value of 0.01 was considered the optimum ccp_alpha parameter. The performance indices for all iterations are presented in Table 7. Although the pruning stage decreases the performance of the training set, the model with ccp_alpha of 0.01 can

yield efficient prediction on a new dataset and be considered the optimum CART model. The structure of the corresponding regression tree is presented in Figure 10.

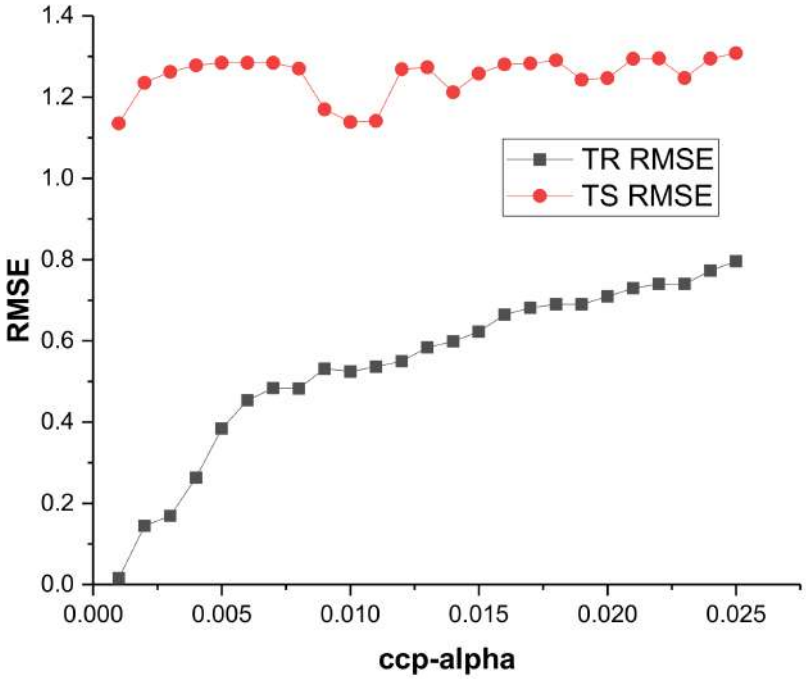

Figure 9. RMSE performance of potential CART models under different ccp_alpha values.

Table 7. Performance metric of CART models under different ccp_alpha values.

ccp_alpha	Training		Testing	
	RMSE	**R^2**	**RMSE**	**R^2**
0.001	0.016	0.890	1.135	0.733
0.002	0.145	0.881	1.235	0.707
0.003	0.169	0.860	1.262	0.701
0.004	0.263	0.858	1.278	0.693
0.005	0.384	0.854	1.284	0.688
0.006	0.454	0.851	1.284	0.680
0.007	0.484	0.844	1.284	0.690
0.008	0.483	0.845	1.270	0.690
0.009	0.531	0.834	1.170	0.680
0.01	**0.524**	**0.834**	**1.139**	**0.744**
0.011	0.536	0.833	1.141	0.742
0.012	0.550	0.813	1.268	0.694
0.013	0.584	0.823	1.273	0.692
0.014	0.599	0.821	1.212	0.716
0.015	0.623	0.816	1.258	0.698
0.016	0.664	0.809	1.280	0.689
0.017	0.681	0.805	1.283	0.689
0.018	0.690	0.804	1.291	0.704
0.019	0.690	0.804	1.243	0.704
0.02	0.709	0.800	1.247	0.702
0.021	0.730	0.796	1.294	0.684
0.022	0.740	0.794	1.295	0.683
0.023	0.740	0.794	1.247	0.702
0.024	0.773	0.787	1.295	0.684
0.025	0.796	0.782	1.308	0.678

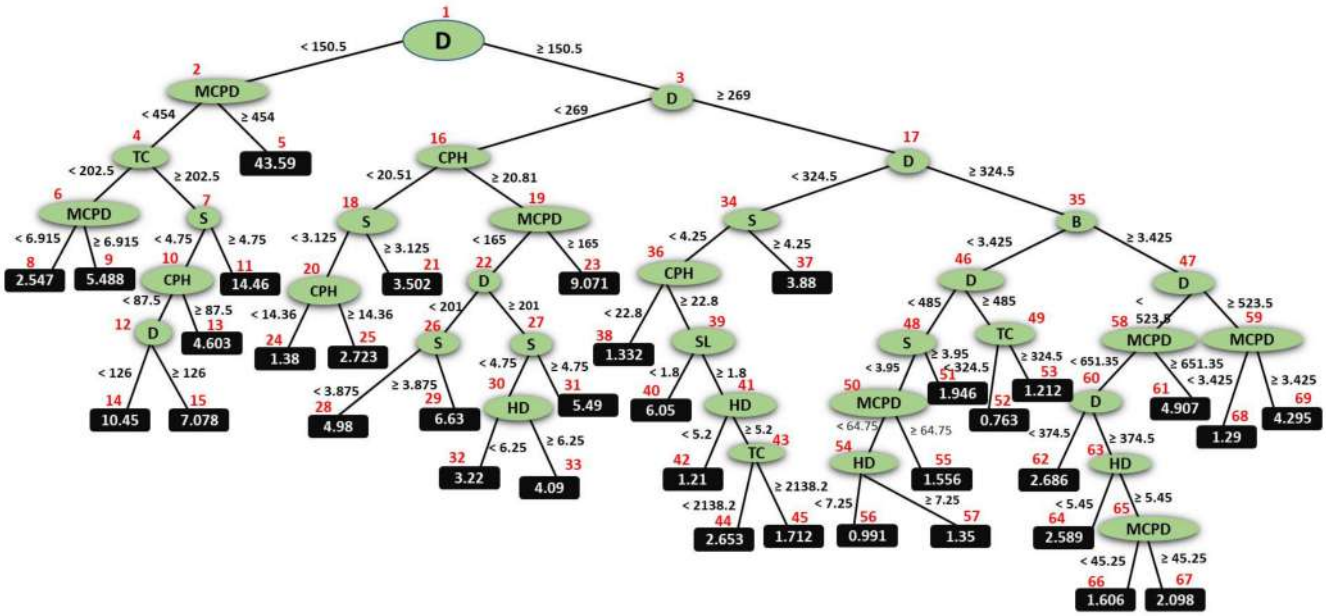

Figure 10. Tree structure for the proposed CART model.

The relationship between the measured and predicted PPV-base CART model is presented in Figure 11 for both training and testing datasets. The proposed CART model with an R^2 of 0.74 on unseen data (test dataset) outperformed the best empirical predictor (Ambraseys–Hendron equation, $R^2 = 0.67$) and multiple linear regression ($R^2 = 0.4$). It can be employed to estimate PPV with a prediction accuracy of over 74%.

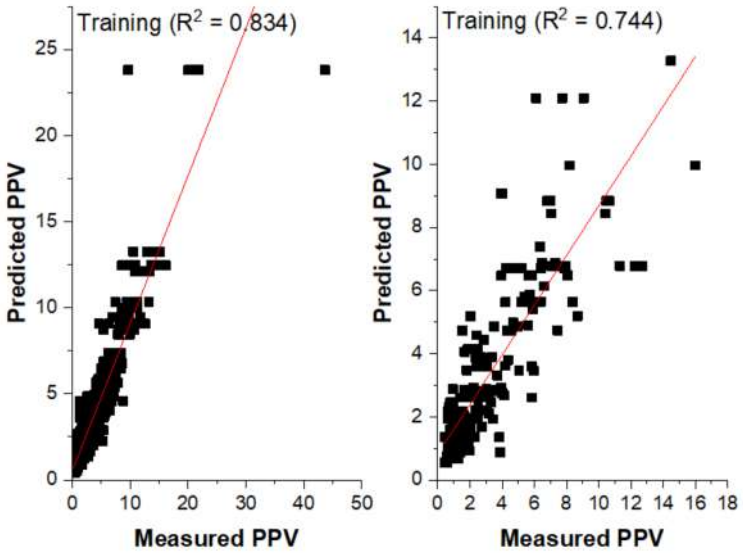

Figure 11. Measured versus Predicted PPV (CART model).

3.4. SVR Model for the Prediction of PPV

In the SVR model, the radial basis function (RBF), which best explains the non-linearity relationship between variables, was employed to establish the model using Python numerical code. Two key hyperparameters including cost–complexity (c) and gamma (δ) govern the SVR model-based RBF kernel function. To obtain the optimum value of 'c', several iterations were performed as presented in Figure 12. The value for which minimum RMSE was attained on the testing dataset was considered the optimum value, which was found to be 32 at the ninth iteration. The final 'c' value was fixed while the other hyper-

parameter gamma (δ) was varied. The RMSE curve change for parameter gamma (δ) on the testing dataset as presented in Figure 13 reveals that the value of gamma (δ) for which minimum error (RMSE = 1.619) is archived is δ = 0.1 and was considered to be the optimum parameter (δ).

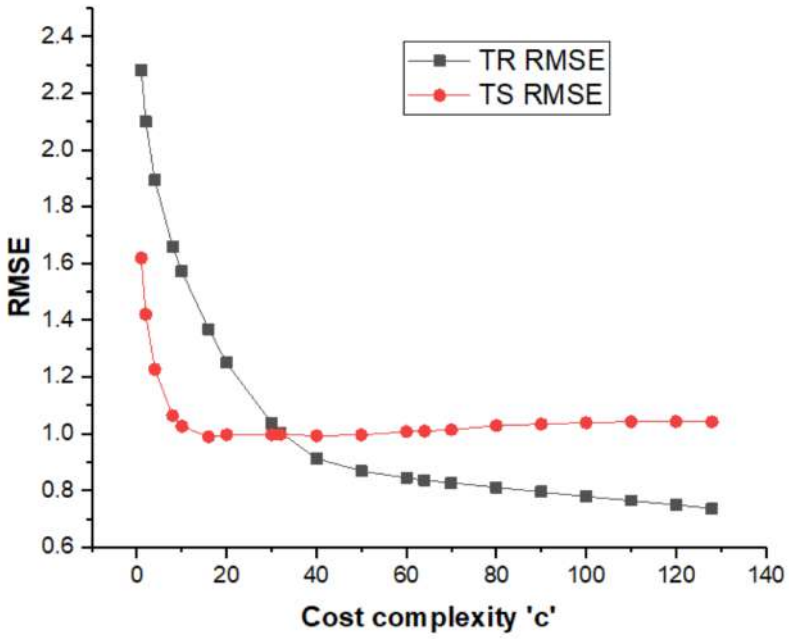

Figure 12. RMSE change curve for cost–complexity 'c' parameter for SVR.

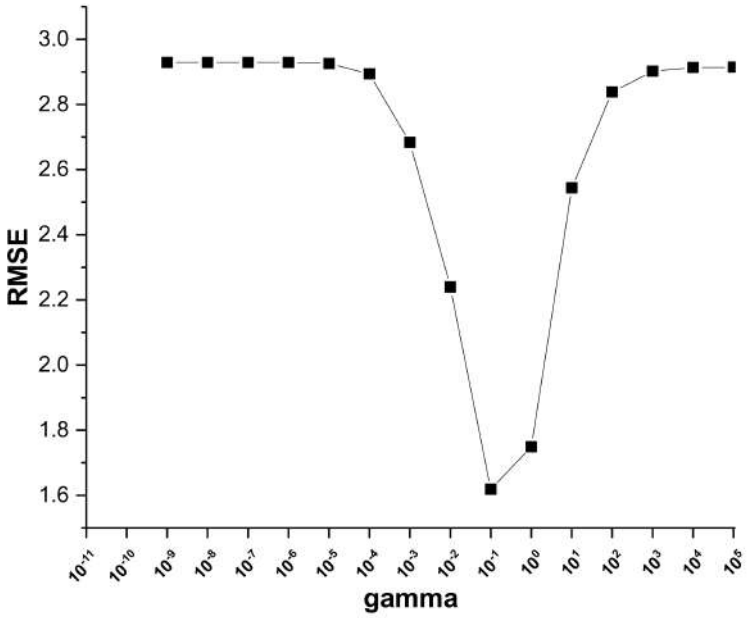

Figure 13. RMSE change curve for gamma parameter.

A summary of the overall SVR models with varying values of 'c' and the optimum gamma δ = 0.1 is presented in Table 8. The proposed model with 'c' = 32 and δ = 0.1 yielded an R^2 and RMSE of 0.9007 and 1.0047 for the training dataset and 0.876 and 0.9981 for testing datasets. The relationship between measured and predicted PPV is presented in Figure 14. The results indicate better accuracy of the SVR model as compared to MLR, empirical, and CART models.

Table 8. Co-efficient of determination R^2 change curves for endspan_alpha and minspan_alpha.

c	Training		Testing		c	Training		Testing	
	RMSE	**R^2**	**RMSE**	**R^2**		**RMSE**	**R^2**	**RMSE**	**R^2**
1	2.2819	0.4879	1.619	0.6739	120	0.7502	0.9446	1.0437	0.8644
2	2.0996	0.5664	1.4207	0.7489	128	0.7367	0.9462	1.0424	0.8648
4	1.8943	0.647	1.2273	0.8126	130	0.7367	0.9466	1.0423	0.8648
8	1.6598	0.729	1.0635	0.8592	140	0.7247	0.9483	1.0441	0.8643
10	1.5724	0.7568	1.0266	0.8688	150	0.7169	0.9494	1.0488	0.8631
16	1.3689	0.8157	0.9896	0.8781	160	0.7054	0.951	1.0555	0.8614
20	1.25	0.8452	0.9966	0.8764	170	0.6945	0.9525	1.0608	0.86
30	1.0378	0.894	0.9967	0.8764	180	0.6844	0.9539	1.0642	0.8591
32	**1.0047**	**0.9007**	**0.9981**	**0.876**	190	0.6749	0.9551	1.0665	0.8584
40	0.9122	0.9181	0.9931	0.8773	200	0.6666	0.9562	1.0685	0.8579
50	0.8694	0.9256	0.9964	0.8764	300	0.6064	0.9638	1.0894	0.8523
60	0.8445	0.9298	1.0073	0.8737	500	0.5691	0.9681	1.1134	0.8457
64	0.8366	0.9311	1.0097	0.8731	1000	0.533	0.972	1.166	0.8308
70	0.8267	0.9327	1.0146	0.8719	5000	0.4513	0.9799	1.3085	0.7869
80	0.8115	0.9352	1.0289	0.8682	10000	0.4189	0.9827	1.3823	0.7622
90	0.7951	0.9378	1.0344	0.8668	50000	0.347	0.9881	2.0686	0.4677
100	0.7789	0.94033	1.0394	0.8656	100000	0.3258	0.9895	2.786	0.3681
110	0.7643	0.9425	1.0431	0.8646					

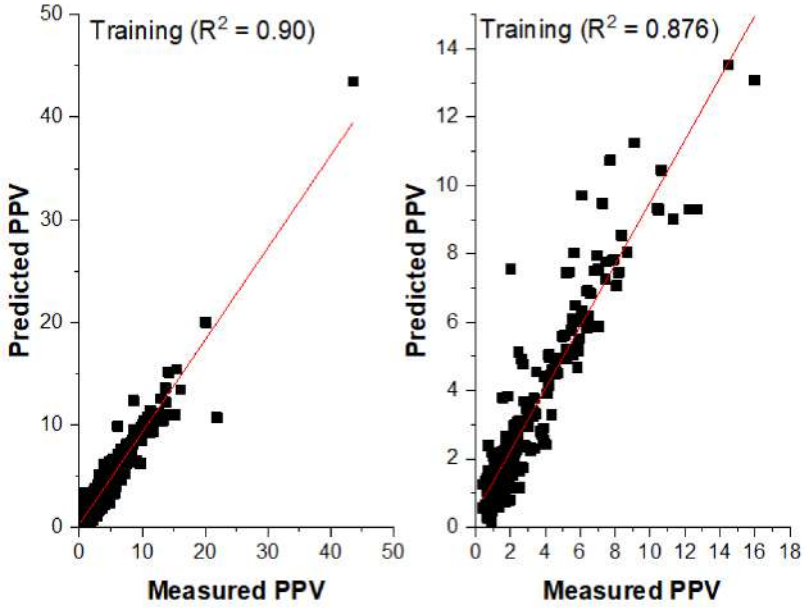

Figure 14. Measured versus Predicted PPV (SVR model).

3.5. MARS Model for the Prediction of PPV

MARS model was trained using the py-earth Python package through the Spyder (Anaconda3) environment. The py-earth library incorporates all the parameters involved in the MARS algorithm as per Friedman [70]. In the training procedure, several iterations were performed using key hyperparameters such as penalty parameter, endspan_alpha, and minspan_alpha. The performance of the developed model during training stage with varying values of the hyperparameters are presented in Figures 15 and 16 for penalty and endspan/minspan_alpha, respectively. From Figure 15, it can be seen that the minimum error (RMSE = 0.227) during the testing stage was obtained at the penalty value of 3.0 and considered the optimum. Then, the parameters endspan_alpha and minspan_alpha were varied consecutively (Table 9), keeping the optimum penalty value constant at 3.0. The value of 0.05 for both parameters yielded the highest performance (R^2 = 0.951) on training

and testing datasets (Figure 16). The optimum hyperparameter values yielded a total of 55 candidate BFs, as shown in Figure 17. It is worth noting that the generalized cross-validation (GCV) method is applied to remove insignificant BFs during the backward stage. Figure 17 indicates 32 prominent numbers of terms with the highest general co-efficient of determination (R^2). The remaining terms (BFs) does not influence the model performance as the R^2 remains relatively unalterable with further BFs (Figure 17). Therefore, the insignificant BFs were removed (pruned) and the final MARS model involves 32 imperative BFs. A similar methodology was employed by Abdulelah Al-Sudani et al. [72] and Chen et al. [73] in previous research to identify the optimum MARS model. The elected 32 BFs and their corresponding coefficients are presented in Table 10 alongside the general regression equation. The application of this equation consists of summing the regression equations of each spline (BF). The obtained value represents the target response PPV based on the proposed MARS model. From Table 9, it can be seen that the performance of both training and testing data are similar, suggesting a good generalization ability of the proposed MARS model.

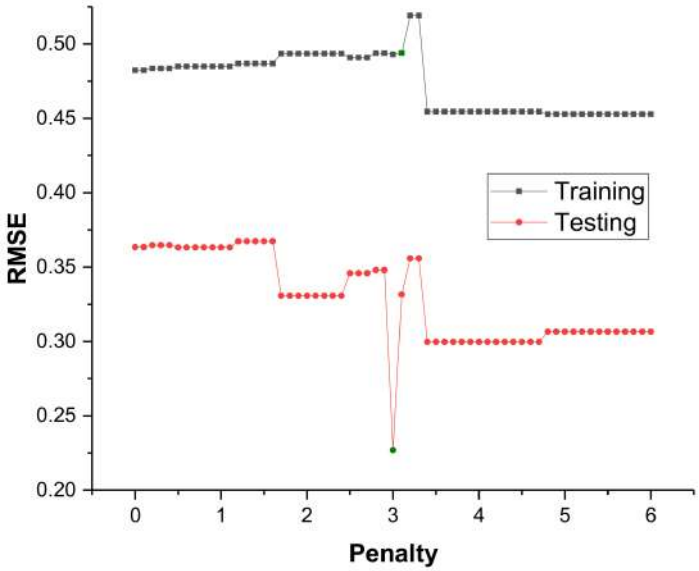

Figure 15. RMSE change curve for penalty parameter.

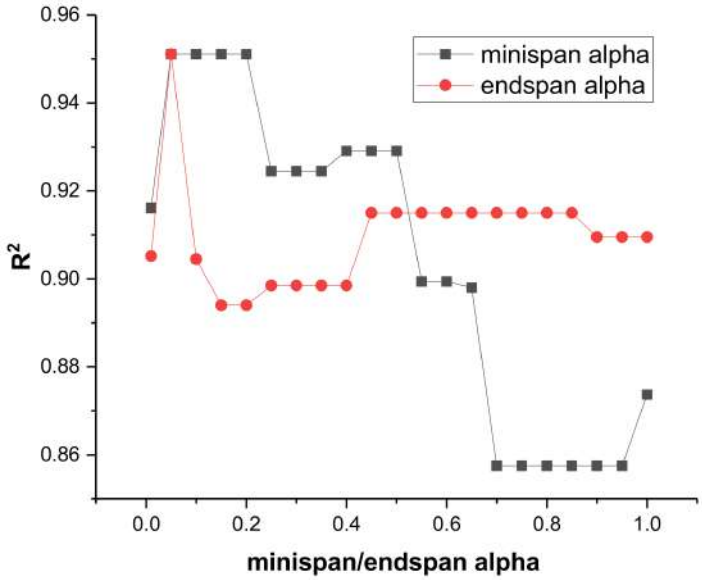

Figure 16. R^2 change curve for minispan alpha and endspan alpha parameter.

Table 9. Performance metrics of different MARS models with varying values of minispan alpha and endspan of alpha.

Minispan/Endspan Alpha	Training		Testing	
	RMSE	**R^2**	**RMSE**	**R^2**
0.01	0.413	0.935	0.601	0.875
0.05	**0.463**	**0.927**	**0.227**	**0.951**
0.1	0.439	0.931	0.476	0.905
0.15	0.440	0.931	0.523	0.894
0.2	0.440	0.931	0.523	0.894
0.25	0.468	0.926	0.559	0.886
0.3	0.468	0.926	0.559	0.886
0.35	0.468	0.926	0.559	0.886
0.4	0.468	0.926	0.559	0.886
0.45	0.440	0.931	0.499	0.899
0.5	0.440	0.931	0.499	0.899
0.55	0.440	0.931	0.499	0.899
0.6	0.425	0.933	0.577	0.881
0.65	0.457	0.928	0.494	0.901
0.7	0.430	0.932	0.599	0.876
0.75	0.456	0.928	0.583	0.880
0.8	0.456	0.928	0.583	0.880
0.85	0.456	0.928	0.583	0.880
0.9	0.488	0.923	0.538	0.891
0.95	0.488	0.923	0.538	0.891
1	0.334	0.947	0.628	0.869

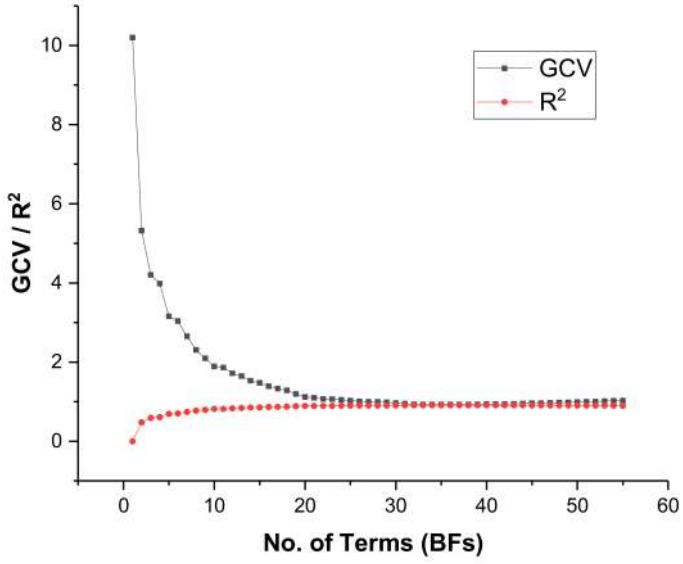

Figure 17. Pruning stage and model selection.

Further analysis is performed to evaluate the importance of the input variables for the MARS model. Figure 18 shows the relative importance of the input parameters expressed as percentages. It can be seen that the monitoring distance (D) and maximum charge per delay (MCPD) are the critical predictors, whereas the number of holes (NH) has the least influence on PPV. This is in line with the results of previous investigations, stating the strong relationship between scaled distance and PPV [74]. The relationship between the predicted and measured PPV based on the proposed MARS model is shown in Figure 19.

Table 10. Effective BFs and the corresponding coefficients.

Basis Function $BF(x)$	Co-Efficient (β_n)	Basis Function $BF(x)$	Co-Efficient (β_n)
Intercept (β_0)	1.960120000	BF17 = h(145−NH)*B*h(341−D)	−0.000145193
BF1 = h(D−341)	−0.002770310	BF18 = SL*TC*h(1130−TC)	−0.000002270
BF2 = h(S−7.5)*h(341−D)	0.402890000	BF19 = MCPD*h(408−D)*h(156.25−CPH)	0.000001079
BF3 = h(10000−TC)*h(341−D)	0.000003126	BF20 = h(NH−145)*B*h(12.25−HD)	0.001295930
BF4 = D*h(341−D)	−0.000149723	BF21 = h(HDM−260)*h(CPH−156.25)	0.001648200
BF5 = TC*h(10000−TC)*h(341−D)	0.000000001	BF22 = h(408−D)	−0.023060800
BF6 = B*h(341−D)	0.018892700	BF23 = D*D*h(341−D)	0.000000465
BF7 = MCPD*h(7.5−S)*h(341−D)	−0.000095901	BF24 = h(S−7.5)*HDM*h(12.25−HD)	−0.002203750
BF8 = MCPD*B*h(341−D)	−0.000123622	BF25 = h(7.5−S)*HDM*h(12.25−HD)	−0.000569359
BF9 = S*h(10000−TC)*h(341−D)	0.000001058	BF26 = HDM*B*h(341−D)	0.000183443
BF10 = h(408−D)*h(156.25−CPH)	−0.000181658	BF27 = SL*HDM*h(12.25−HD)	0.000580015
BF11 = HD*h(408−D)*h(156.25−CPH)	0.000017127	BF28 = MCPD*h(341−D)	0.000683227
BF12 = h(145−NH)*h(408−D)*h(156.25−CPH)	0.000002181	BF29 = SL*B*h(341−D)	−0.002187630
BF13 = TC*h(1130−TC)	0.000008631	BF30 = B*B*h(341−D)	−0.003844060
BF14 = HDM*h(1130−TC)	−0.000025563	BF31 = HDM*h(10000−TC)*h(341−D)	−0.000000028
BF15 = HDM*HDM*h(1130−TC)	0.000000146	BF32 = HDM*D*h(341−D)	−0.000001313
BF16 = h(NH−145)*B*h(341−D)	−0.001396160		
Resulting expression		$PPV = \beta_0 + \sum_{n=1}^{n=N} \beta_n BF(x)$	

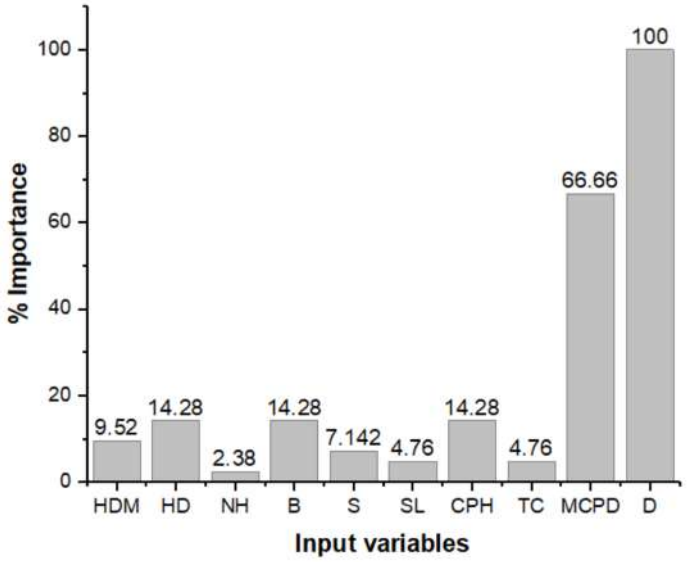

Figure 18. Predictor importance analysis for MARS model.

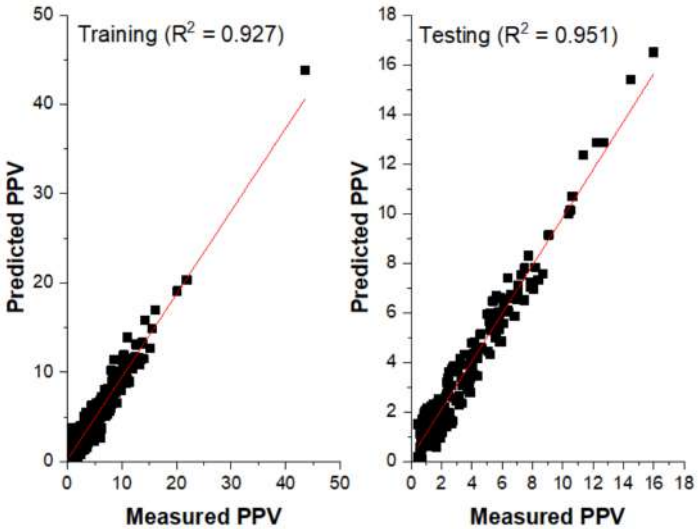

Figure 19. Measured versus Predicted PPV (MARS model).

4. Discussion

Predicting PPV is one technique to minimize the damage induced by rock-blasting vibration in mines. PPV is influenced by various blasting parameters. The ability to identify the most influential factors is key to building a good predictive model. This study uses cosine amplitude and observes the influence of rock-blasting parameters on the induced PPV. These include hole diameter, hole depth, number of holes, burden, spacing, stemming length, charge per hole, total charge, maximum charge per delay, and monitoring distance. These parameters diversely influence PPV and have been used by various researchers to develop PPV predictive models based on machine-learning technique [9,42,75]. Machine learning is extensively used to solve several prediction problems because of its accuracy as compared to empirical and statistical methods. The prediction accuracy depends upon the techniques employed and inter-correlation between input and output variables. It has been observed that a model generalization ability increases with the input variables and the number of datasets. Recently, hybrid models have been introduced to increase prediction accuracy. However, these models are difficult to interpret and implement by practitioners in the field. White-box ML techniques such as MARS and CART can provide reasonable prediction accuracy and are easily implementable. This study develops a simple ML model that can be easily used by field practitioners to predict PPV. Many datasets from various geo-environments have been involved to develop conventional ML models to increase generalization ability. The models were well trained based on a trial-and-error approach to obtain the best fitting with minimum error for PPV prediction. Three ML techniques, including MARS, CART and SVR, were employed in this study, and the results were compared to conventional statistical methods and empirical predictors. The performance of all developed models for both training and testing sets is reported in Table 11. As can be seen, the best performances were obtained through machine-learning techniques. This confirms that the relationships between the influential parameters and the PPV are non-linear.

Table 11. Performance indices of the proposed models for predicting PPV.

Model	Training		Testing	
	RMSE	**R^2**	**RMSE**	**R^2**
USBM	2.369	0.489	0.918	0.630
Langefors–Kihlstrom	2.370	0.001	1.405	0.096
Ambraseys–Hendron	2.328	0.493	0.855	0.673
ISI	3.213	0.144	1.324	0.223
CMRI predictor	2.318	0.482	0.890	0.621
MLR	2.503	0.384	1.095	0.400
CART	0.524	0.834	1.138	0.744
SVR	1.005	0.90	0.998	0.876
MARS	0.463	0.927	0.227	0.951

For a more convenient comparison and model performance assessment, a Taylor diagram was established, as shown in Figure 20. From Figure 20, it can be seen that ML models are the nearest to the reference point. This indicates that these models agree well with the actual observation [76]. According to the presented result (Figure 20), the MARS model indisputably agrees best with the observations, as it yielded the lowest centered root-mean-square difference (RMS) and highest correlation co-efficient. This observation compared well with the results presented in Table 11, which showed that the proposed MARS model discloses superior performance in this study. The model can be adopted in predicting PPV resulting from blasting in opencast mines. A similar method was employed to compare and assess the best machine-learning model in predicting blast-induced air overpressure [77].

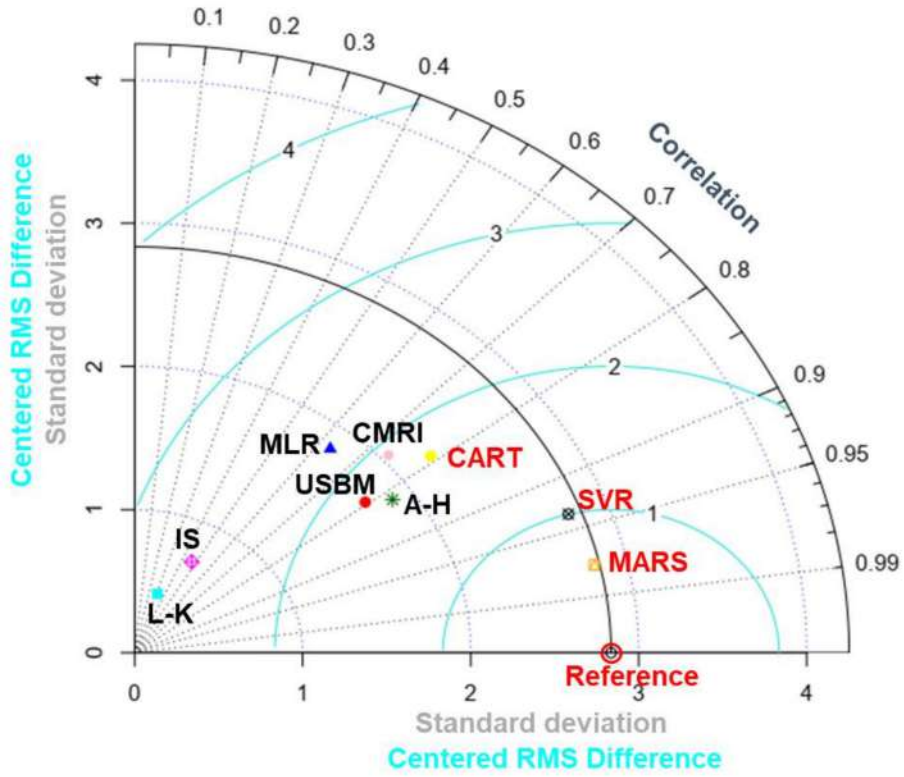

Figure 20. Comparison of the proposed model performances using a Taylor diagram.

The MARS model outperformed all other developed models. It is reported that the performance of a model on unseen data (test data) with respect to the training dataset is an indicator to evaluate model generalization ability. As shown in Table 11, the performance of the proposed MARS model on the training set and the testing set do not differ significantly, and the prediction error (RMSE) was the lowest. This indicates the strong generalization ability of the MARS model as compared to SVR and CART. Furthermore, the MARS model provides the interactive behavior between variables. The input variables (basis function (BFs)) with their corresponding co-efficient from the MARS model led to the general equation for the prediction of PPV (Table 10). Although the SVR model outperformed the CART model (Table 11), the latter has the advantage of easy interpretability. The tree generated by the CART model can be used as a benchmark for the optimization process based on trial-and-error experimentation. It is worth noting that except for the MARS model, the accuracy of the proposed models underperformed some models available in the literature (Table 1). This might be attributed to the high number of input variables and datasets, which increases the complexity of the models [8]. However, it is reported that many datasets and input variables enhance the generalization ability of regression models [12]. To the best knowledge of the authors, there are no existing models involving many blasting events and input variables as in the case of the present study. It suggests that the proposed models will better estimate PPV in practical engineering with reasonable accuracy than other existing models developed with fewer variables and datasets. The proposed model involved only blast-design parameters, and has the advantage of applying it in areas where rock (mass) properties are difficult to obtain. However, further investigations should be carried out involving both blasting parameters and rock (mass) properties with large datasets to ensure the generalization ability of the models.

5. Conclusions

Ground vibration is one of the inevitable adverse effects induced by rock blasting. Peak particle velocity (PPV) is the universally used parameter to assess blast-induced damages. Predicting PPV is the only way to prevent and reduce the damages induced by blasting

vibration. This study applied machine-learning techniques to develop a generalized and interpretable model for PPV estimation. CART and MARS, as white-box ML techniques, have the advantage of easy interpretability and application and were employed in this study. Furthermore, a black-box SVR algorithm, as well as multiple linear regression and conventional empirical predictors, were applied and compared to CART and MARS models. Several conclusions from the presented study can be drawn as follows:

- Based on 1001 datasets, the effective parameters on PPV were assessed using sensitivity analysis. PPV depends upon various blast-design parameters such as hole diameter, hole depth, number of holes, burden, spacing, stemming length, charge per hole, total charge, maximum charge per delay, and monitoring distance.
- Machine-learning techniques outperformed traditional prediction techniques including empirical and statistical methods and better explain the non-linear interaction between input variables and the response PPV.
- A comprehensive quantitative interaction between input variables and the response PPV is obtained from CART and MARS models, and can be easily employed to predict PPV with reasonable accuracy.
- Despite using many datasets and input variables, the study shows that the MARS model can be easily employed to estimate PPV with high prediction accuracy (R^2 = 0.951; RMSE = 0.227) compared to CART and SVR.

Author Contributions: Conceptualization, A.R. and G.C.K.; Data curation, G.J.; Formal analysis, A.R.; Funding acquisition, P.A.O.; Methodology, G.C.K.; Project administration, C.S.; Resources, P.A.O.; Software, G.C.K. and G.J.; Supervision, A.R. and V.A.; Validation, L.A.G., V.A., A.R. and C.S.; Visualization, A.R.; Writing—original draft, G.C.K.; Writing—review & editing, A.R., L.A.G., V.A. and P.A.O.; Materials, C.S. All authors have read and agreed to the published version of the manuscript.

Funding: This work was supported by Council of Scientific and Industrial Research-Central Institute of Mining and Fuel Research (CSIR-CIMFR), Dhanbad, India. And supported by CSIR-The World Academy of Science (TWAS) and the Partnership for skills in Applied Sciences, Engineering and Technology (PASET).

Institutional Review Board Statement: Not applicable.

Informed Consent Statement: Not applicable.

Data Availability Statement: The data are available upon request.

Conflicts of Interest: The authors declare no conflict of interest.

Abbreviations

ABS	Absorption	**MCPD**	Maximum charge per delay
AGPSO	Autonomous groups particles swarm optimization	**MFA**	Modified firefly algorithm
A–H	Ambraseys–Hendron predictors	**MFA**	Modified firefly algorithm
ANFIS	Adaptive neuro-fuzzy inference system	**MFO**	Moth-flame optimization algorithm
ANN	Artificial neural network	**MIV**	Mean impact value
B	Burden	**ML**	Machine learning
BCPRA	Blast-control point relative angle	**MLPNN**	Multilayer perceptrons neural network
BF	Basis function	**MLR**	Multiple linear regression;
BI	Blasting index	**MPMR**	Minimax probability machine regression
BIGV	Blast-induced ground vibration	**MR**	Multiple regression;
BK	Buckingham π (pi) theorem	**MVRA**	Multivariate regression analysis
BP	Backpropagation	**NDS**	Number of blasting groups
BPNN	Backpropagation neural network	**NH**	Number of holes
CART	Classification and regression tree	**NHPD**	Number of holes per delay
CL	Average charge length	**NLMR**	Non-linear multiple regression

CMRI	Central Mining Research Institute predictor	**NR**	Number of rows
CPH	Average explosive charge per hole	**PF**	Powder factor
CRANFIS	Chaos recurrent adaptive neuro-fuzzy inference system	**PLI**	Point load index
CSO	Cuckoo search optimization	**PPV**	Peak particle velocity
D	Distance	**PSO**	Particle swarm optimization
DPR	Delay per row	**P-wave**	P-wave velocity
DTS	Time delay for each group,	**R^2**	Co-efficient of determination
E	Young's modulus	**RANFIS**	Recurrent adaptive neuro-fuzzy inference system
ELM	Extreme learning machine	**RBFNN**	Radial basis function neural network
FA	Firefly algorithm	**Rdis**	Radial distances
FRC	Fracture roughness co-efficient	**RF**	Random forest
FS	Fuzzy system	**RMR**	Rock mass rating
GA	Genetic algorithm	**RMSE**	Root-mean-square error
GCV	Generalized cross-validation	**RQD**	Rock quality designation
GEP	Gene-expression programming	**S**	Spacing
GFFN	Generalized feed-forward neural network	**SCA**	Sine cosine algorithm
G–D	Ghosh–Daemen empirical predictor	**SD**	Sub-drilling;
GMDH	Group method of data handling	**SL**	Steaming length
GOA	Grasshopper optimization algorithm	**SRH**	Schmidt rebound hardness value
GPR	Gaussian process regression	**SVM**	Support vector machine
GRNN	General regression neural network	**SVR**	Support vector regression
H	Bench height	**TC**	Total charge
Hc	Hardness co-efficient	**TS**	Tunnel cross-section
HD	Hole depth	**UCS**	Uniaxial compressive strength
Hdis	Horizontal distances	**USBM**	United states bureau of mines
HDM	Hole diameter	**Ve**	Volume of extracted block
HGS	Hunger games search	**VOD**	Velocity of detonation
HHO	Harris hawks optimization	**XGBoost**	Extreme gradient boosting
ICA	Imperialist competitive algorithm	**ρe**	Explosive density
IS	Indian standard predictor	**ρr**	Rock density
L–K	Langefors–Kihlstrom predictor	η	Porosity
LSSVM	Least-squares support vector machine	**μ**	Poisson ratio
MARS	Multivariate adaptive regression splines		

References

1. Bayat, P.; Monjezi, M.; Mehrdanesh, A.; Khandelwal, M. Blasting pattern optimization using gene expression programming and grasshopper optimization algorithm to minimise blast-induced ground vibrations. *Eng. Comput.* **2021**, *38*, 3341–3350. [CrossRef]
2. Siskind, D.E.; Strachura, V.J.; Stagg, M.S.; Kopp, J.W. *Structure Response and Damage Produced by Airblast from Surface Mining*; US Department of the Interior, Bureau of Mines: Washington, DC, USA, 1980.
3. Lawal, A.I.; Kwon, S.; Kim, G.Y. Prediction of the blast-induced ground vibration in tunnel blasting using ANN, moth-flame optimized ANN, and gene expression programming. *Acta Geophys.* **2021**, *69*, 161–174. [CrossRef]
4. Dumakor-Dupey, N.; Arya, S.; Jha, A. Advances in Blast-Induced Impact Prediction—A Review of Machine Learning Applications. *Minerals* **2021**, *11*, 601. [CrossRef]
5. Yan, Y.; Hou, X.; Fei, H. Review of predicting the blast-induced ground vibrations to reduce impacts on ambient urban communities. *J. Clean. Prod.* **2020**, *260*, 121135. [CrossRef]
6. Ghoraba, S.; Monjezi, M.; Talebi, N.; Armaghani, D.J.; Moghaddam, M.R. Estimation of ground vibration produced by blasting operations through intelligent and empirical models. *Environ. Earth Sci.* **2016**, *75*, 1137. [CrossRef]
7. Faradonbeh, R.S.; Monjezi, M. Prediction and minimization of blast-induced ground vibration using two robust meta-heuristic algorithms. *Eng. Comput.* **2017**, *33*, 835–851. [CrossRef]

8. Xu, S.; Li, Y.; Liu, J.; Zhang, F. Optimization of blasting parameters for an underground mine through prediction of blasting vibration. *J. Vib. Control* **2019**, *25*, 1585–1595. [CrossRef]
9. Bayat, P.; Monjezi, M.; Rezakhah, M.; Armaghani, D.J. Artificial Neural Network and Firefly Algorithm for Estimation and Minimization of Ground Vibration Induced by Blasting in a Mine. *Nat. Resour. Res.* **2020**, *29*, 4121–4132. [CrossRef]
10. Giustolisi, O. Using genetic programming to determine Chezy resistance coefficient in corrugated channels. *J. Hydroinform.* **2004**, *6*, 157–173. [CrossRef]
11. Rudin, C. Stop explaining black box machine learning models for high stakes decisions and use interpretable models instead. *Nat. Mach. Intell.* **2019**, *1*, 206–215. [CrossRef]
12. Monjezi, M.; Hasanipanah, M.; Khandelwal, M. Evaluation and prediction of blast-induced ground vibration at Shur River Dam, Iran, by artificial neural network. *Neural Comput. Appl.* **2013**, *22*, 1637–1643. [CrossRef]
13. Ke, B.; Nguyen, H.; Bui, X.-N.; Costache, R. Estimation of Ground Vibration Intensity Induced by Mine Blasting using a State-of-the-Art Hybrid Autoencoder Neural Network and Support Vector Regression Model. *Nat. Resour. Res.* **2021**, *30*, 3853–3864. [CrossRef]
14. Nguyen, H.; Bui, X.-N. A Novel Hunger Games Search Optimization-Based Artificial Neural Network for Predicting Ground Vibration Intensity Induced by Mine Blasting. *Nat. Resour. Res.* **2021**, *30*, 3865–3880. [CrossRef]
15. Singh, T. Artificial neural network approach for prediction and control of ground vibrations in mines. *Min. Technol.* **2004**, *113*, 251–256. [CrossRef]
16. Nguyen, H.; Bui, X.-N.; Tran, Q.-H.; Nguyen, H.A.; Nguyen, D.-A.; Hoa, L.T.T.; Le, Q.-T. Prediction of ground vibration intensity in mine blasting using the novel hybrid MARS–PSO–MLP model. *Eng. Comput.* **2021**. [CrossRef]
17. Singh, T.N.; Dontha, L.K.; Bhardwaj, V. Study into blast vibration and frequency using ANFIS and MVRA. *Min. Technol.* **2008**, *117*, 116–121. [CrossRef]
18. Lawal, A.I.; Olajuyi, S.I.; Kwon, S.; Onifade, M. A comparative application of the Buckingham π (pi) theorem, white-box ANN, gene expression programming, and multilinear regression approaches for blast-induced ground vibration prediction. *Arab. J. Geosci.* **2021**, *14*, 1073. [CrossRef]
19. Singh, T.N.; Verma, A.K. Sensitivity of total charge and maximum charge per delay on ground vibration. *Geomat. Nat. Hazards Risk* **2010**, *1*, 259–272. [CrossRef]
20. Monjezi, M.; Ghafurikalajahi, M.; Bahrami, A. Prediction of blast-induced ground vibration using artificial neural networks. *Tunn. Undergr. Space Technol.* **2011**, *26*, 46–50. [CrossRef]
21. Khandelwal, M.; Singh, T. Prediction of blast-induced ground vibration using artificial neural network. *Int. J. Rock Mech. Min. Sci.* **2009**, *46*, 1214–1222. [CrossRef]
22. Khandelwal, M. Evaluation and prediction of blast-induced ground vibration using support vector machine. *Int. J. Rock Mech. Min. Sci.* **2010**, *47*, 509–516. [CrossRef]
23. Khandelwal, M.; Singh, T. Evaluation of blast-induced ground vibration predictors. *Soil Dyn. Earthq. Eng.* **2007**, *27*, 116–125. [CrossRef]
24. Monjezi, M.; Ahmadi, M.; Sheikhan, M.; Bahrami, A.; Salimi, A. Predicting blast-induced ground vibration using various types of neural networks. *Soil Dyn. Earthq. Eng.* **2010**, *30*, 1233–1236. [CrossRef]
25. Yu, C.; Koopialipoor, M.; Murlidhar, B.R.; Mohammed, A.S.; Armaghani, D.J.; Mohamad, E.T.; Wang, Z. Optimal ELM–Harris Hawks Optimization and ELM–Grasshopper Optimization Models to Forecast Peak Particle Velocity Resulting from Mine Blasting. *Nat. Resour. Res.* **2021**, *30*, 2647–2662. [CrossRef]
26. Mohamed, M.T. Performance of fuzzy logic and artificial neural network in prediction of ground and air vibrations. *Int. J. Rock Mech. Min. Sci.* **2011**, *48*, 845–851. [CrossRef]
27. Khandelwal, M.; Kumar, D.L.; Yellishetty, M. Application of soft computing to predict blast-induced ground vibration. *Eng. Comput.* **2011**, *27*, 117–125. [CrossRef]
28. Singh, J.; Verma, A.K.; Banka, H.; Singh, T.N.; Maheshwar, S. A study of soft computing models for prediction of longitudinal wave velocity. *Arab. J. Geosci.* **2016**, *9*, 224. [CrossRef]
29. Zhou, J.; Qiu, Y.; Khandelwal, M.; Zhu, S.; Zhang, X. Developing a hybrid model of Jaya algorithm-based extreme gradient boosting machine to estimate blast-induced ground vibrations. *Int. J. Rock Mech. Min. Sci.* **2021**, *145*, 104856. [CrossRef]
30. Mohamed, M.T. Artificial neural network for prediction and control of blasting vibrations in Assiut (Egypt) limestone quarry. *Int. J. Rock Mech. Min. Sci.* **2009**, *46*, 426–431. [CrossRef]
31. Rana, A.; Bhagat, N.K.; Jadaun, G.P.; Rukhaiyar, S.; Pain, A.; Singh, P.K. Predicting Blast-Induced Ground Vibrations in Some Indian Tunnels: A Comparison of Decision Tree, Artificial Neural Network and Multivariate Regression Methods. *Min. Met. Explor.* **2020**, *37*, 1039–1053. [CrossRef]
32. Verma, A.; Singh, T.N. Comparative study of cognitive systems for ground vibration measurements. *Neural Comput. Appl.* **2013**, *22*, 341–350. [CrossRef]
33. Verma, A.K.; Singh, T.N. Intelligent systems for ground vibration measurement: A comparative study. *Eng. Comput.* **2011**, *27*, 225–233. [CrossRef]
34. Ghasemi, E.; Ataei, M.; Hashemolhosseini, H. Development of a fuzzy model for predicting ground vibration caused by rock blasting in surface mining. *J. Vib. Control* **2013**, *19*, 755–770. [CrossRef]

35. Ghasemi, E.; Kalhori, H.; Bagherpour, R. A new hybrid ANFIS–PSO model for prediction of peak particle velocity due to bench blasting. *Eng. Comput.* **2016**, *32*, 607–614. [CrossRef]
36. Bui, X.-N.; Nguyen, H.; Tran, Q.-H.; Nguyen, D.-A.; Bui, H.-B. Predicting Ground Vibrations Due to Mine Blasting Using a Novel Artificial Neural Network-Based Cuckoo Search Optimization. *Nat. Resour. Res.* **2021**, *30*, 2663–2685. [CrossRef]
37. Dehghani, H.; Ataee-Pour, M. Development of a model to predict peak particle velocity in a blasting operation. *Int. J. Rock Mech. Min. Sci.* **2011**, *48*, 51–58. [CrossRef]
38. Zhongya, Z.; Xiaoguang, J. Prediction of Peak Velocity of Blasting Vibration Based on Artificial Neural Network Optimized by Dimensionality Reduction of FA-MIV. *Math. Probl. Eng.* **2018**, *2018*, 8473547. [CrossRef]
39. Armaghani, D.J.; Kumar, D.; Samui, P.; Hasanipanah, M.; Roy, B. A novel approach for forecasting of ground vibrations resulting from blasting: Modified particle swarm optimization coupled extreme learning machine. *Eng. Comput.* **2021**, *37*, 3221–3235. [CrossRef]
40. Faradonbeh, R.S.; Armaghani, D.J.; Monjezi, M.; Mohamad, E.T. Genetic programming and gene expression programming for flyrock assessment due to mine blasting. *Int. J. Rock Mech. Min. Sci.* **2016**, *88*, 254–264. [CrossRef]
41. Mokfi, T.; Shahnazar, A.; Bakhshayeshi, I.; Derakhsh, A.M.; Tabrizi, O. Proposing of a new soft computing-based model to predict peak particle velocity induced by blasting. *Eng. Comput.* **2018**, *34*, 881–888. [CrossRef]
42. Lawal, A.I.; Kwon, S.; Hammed, O.S.; Idris, M.A. Blast-induced ground vibration prediction in granite quarries: An application of gene expression programming, ANFIS, and sine cosine algorithm optimized ANN. *Int. J. Min. Sci. Technol.* **2021**, *31*, 265–277. [CrossRef]
43. Hajihassani, M.; Armaghani, D.J.; Marto, A.; Mohamad, E.T. Vibrations au sol prédiction dans quarry dynamitage à travers un réseau neural artificiel optimisé par une concurrence impérialiste algorithme. *Bull. Eng. Geol. Environ.* **2015**, *74*, 873–886. [CrossRef]
44. Chen, W.; Hasanipanah, M.; Rad, H.N.; Armaghani, D.J.; Tahir, M.M. A new design of evolutionary hybrid optimization of SVR model in predicting the blast-induced ground vibration. *Eng. Comput.* **2021**, *37*, 1455–1471. [CrossRef]
45. Peng, K.; Zeng, J.; Armaghani, D.J.; Hasanipanah, M.; Chen, Q. A Novel Combination of Gradient Boosted Tree and Optimized ANN Models for Forecasting Ground Vibration Due to Quarry Blasting. *Nat. Resour. Res.* **2021**, *30*, 4657–4671. [CrossRef]
46. Hasanipanah, M.; Faradonbeh, R.S.; Amnieh, H.B.; Armaghani, D.J.; Monjezi, M. Forecasting blast-induced ground vibration developing a CART model. *Eng. Comput.* **2016**, *33*, 307–316. [CrossRef]
47. Hudaverdi, T.; Akyildiz, O. Prediction and evaluation of blast-induced ground vibrations for structural damage and human response. *Arab. J. Geosci.* **2021**, *14*, 378. [CrossRef]
48. Zhu, W.; Rad, H.N.; Hasanipanah, M. A chaos recurrent ANFIS optimized by PSO to predict ground vibration generated in rock blasting. *Appl. Soft Comput.* **2021**, *108*, 107434. [CrossRef]
49. Shahnazar, A.; Rad, H.N.; Hasanipanah, M.; Tahir, M.M.; Jahed Armaghani, D.; Ghoroqi, M. A new developed approach for the prediction of ground vibration using a hybrid PSO-optimized ANFIS-based model. *Environ. Earth Sci.* **2017**, *76*, 527. [CrossRef]
50. Hasanipanah, M.; Monjezi, M.; Shahnazar, A.; Jahed Armaghani, D.; Farazmand, A. Feasibility of indirect determination of blast induced ground vibration based on support vector machine. *Meas. J. Int. Meas. Confed.* **2015**, *75*, 289–297. [CrossRef]
51. Shahri, A.A.; Pashamohammadi, F.; Asheghi, R.; Shahri, H.A. Automated intelligent hybrid computing schemes to predict blasting induced ground vibration. *Eng. Comput.* **2021**, 1–5. [CrossRef]
52. Saadat, M.; Khandelwal, M.; Monjezi, M. An ANN-based approach to predict blast-induced ground vibration of Gol-E-Gohar iron ore mine, Iran. *J. Rock Mech. Geotech. Eng.* **2014**, *6*, 67–76. [CrossRef]
53. Álvarez-Vigil, A.E.; González-Nicieza, C.; López Gayarre, F.; Álvarez-Fernández, M.I. Predicting blasting propagation velocity and vibration frequency using artificial neural networks. *Int. J. Rock Mech. Min. Sci.* **2012**, *55*, 108–116. [CrossRef]
54. Amini, H.; Gholami, R.; Monjezi, M.; Torabi, S.R.; Zadhesh, J. Evaluation of flyrock phenomenon due to blasting operation by support vector machine. *Neural Comput. Appl.* **2012**, *21*, 2077–2085. [CrossRef]
55. Khandelwal, M.; Armaghani, D.J.; Faradonbeh, R.S.; Yellishetty, M.; Majid, M.Z.A.; Monjezi, M. Classification and regression tree technique in estimating peak particle velocity caused by blasting. *Eng. Comput.* **2017**, *33*, 45–53. [CrossRef]
56. Iphar, M.; Yavuz, M.; Ak, H. Prediction of ground vibrations resulting from the blasting operations in an open-pit mine by adaptive neuro-fuzzy inference system. *Environ. Earth Sci.* **2008**, *56*, 97–107. [CrossRef]
57. Armaghani, D.J.; Hajihassani, M.; Mohamad, E.T.; Marto, A.; Noorani, S.A. Blasting-induced flyrock and ground vibration prediction through an expert artificial neural network based on particle swarm optimization. *Arab. J. Geosci.* **2013**, *7*, 5383–5396. [CrossRef]
58. Lapčević, R.; Kostić, S.; Pantović, R.; Vasović, N. Prediction of blast-induced ground motion in a copper mine. *Int. J. Rock Mech. Min. Sci.* **2014**, *69*, 19–25. [CrossRef]
59. Mohamadnejad, M.; Gholami, R.; Ataei, M. Comparison of intelligence science techniques and empirical methods for prediction of blasting vibrations. *Tunn. Undergr. Space Technol.* **2012**, *28*, 238–244. [CrossRef]
60. Monjezi, M.; Baghestani, M.; Faradonbeh, R.S.; Saghand, M.P.; Armaghani, D.J. Modification and prediction of blast-induced ground vibrations based on both empirical and computational techniques. *Eng. Comput.* **2016**, *32*, 717–728. [CrossRef]
61. Li, D.T.; Yan, J.L.; Zhang, L. Prediction of Blast-Induced Ground Vibration Using Support Vector Machine by Tunnel Excavation. *Appl. Mech. Mater.* **2012**, *170–173*, 1414–1418. [CrossRef]

62. Vasović, D.; Kostić, S.; Ravilić, M.; Trajković, S. Environmental impact of blasting at Drenovac limestone quarry (Serbia). *Environ. Earth Sci.* **2014**, *72*, 3915–3928. [CrossRef]
63. Ragam, P.; Nimaje, D.S. Assessment of blast-induced ground vibration using different predictor approaches—A comparison. *Chem. Eng. Trans.* **2018**, *66*, 487–492. [CrossRef]
64. Yang, Y.; Zhang, Q. A hierarchical analysis for rock engineering using artificial neural networks. *Rock Mech. Rock Eng.* **1997**, *30*, 207–222. [CrossRef]
65. Breiman, L.; Friedman, J.H.; Olshen, R.A.; Stone, C.J. *Classification and Regression Trees*; Routledge: London, UK, 1984.
66. Hastie, T.; Jerome, F.; Tibshirani, R. *The Elements of Statistical Learning Data Mining, Inference, and Prediction*, 2nd ed.; Springer: Stanford, CA, USA, 2008.
67. Ramesh Murlidhar, B.; Yazdani Bejarbaneh, B.; Jahed Armaghani, D.; Mohammed, A.S.; Tonnizam Mohamad, E. Application of tree-based predictive models to forecast air overpressure induced by mine blasting. *Nat. Resources Res.* **2021**, *30*, 1865–1887. [CrossRef]
68. Cortes, C.; Vladimir, V. Support-vector networks. Machine learning. *IEEE Expert Syst. Appl.* **1995**, *20*, 273–297. [CrossRef]
69. Zhang, W.; Goh, A. Multivariate adaptive regression splines for analysis of geotechnical engineering systems. *Comput. Geotech.* **2013**, *48*, 82–95. [CrossRef]
70. Friedman, J.H.T. Multivariate adaptive regression splines. *Ann. Stat.* **1991**, *19*, 1–67. [CrossRef]
71. Gharineiat, Z.; Deng, X. Application of the Multi-Adaptive Regression Splines to Integrate Sea Level Data from Altimetry and Tide Gauges for Monitoring Extreme Sea Level Events. *Mar. Geod.* **2015**, *38*, 261–276. [CrossRef]
72. Al-Sudani, Z.A.; Salih, S.Q.; Sharafati, A.; Yaseen, Z.M. Development of multivariate adaptive regression spline integrated with differential evolution model for streamflow simulation. *J. Hydrol.* **2019**, *573*, 1–12. [CrossRef]
73. Chen, Z.; Li, H.; Goh, A.; Wu, C.; Zhang, W. Soil Liquefaction Assessment Using Soft Computing Approaches Based on Capacity Energy Concept. *Geosciences* **2020**, *10*, 330. [CrossRef]
74. Jimeno, C.L.; Jimeno, E.L.; Carcedo, F.J.A.; De Ramiro, Y.V. *Drilling and Blasting of Rocks*; Routledge: London, UK, 2017.
75. Choi, Y.-H.; Lee, S.S. Predictive Modelling for Blasting-Induced Vibrations from Open-Pit Excavations. *Appl. Sci.* **2021**, *11*, 7487. [CrossRef]
76. Taylor, K.E. Summarizing multiple aspects of model performance in a single diagram. *J. Geophys. Res. Atmos.* **2001**, *106*, 7183–7192. [CrossRef]
77. He, Z.; Armaghani, D.J.; Masoumnezhad, M.; Khandelwal, M.; Zhou, J.; Murlidhar, B.R. A Combination of Expert-Based System and Advanced Decision-Tree Algorithms to Predict Air-Overpressure Resulting from Quarry Blasting. *Nat. Resour. Res.* **2021**, *30*, 1889–1903. [CrossRef]